Layer-specific microglia activation drives chronic stress-induced synapse loss

Authors: Breeanne M. Soteros[1], Haven Tillmon[1], Mackenna Wollet[2], Julianne General[1], Hanna Chin[5], John Beichen Lee[3], Flavia R. Carreno[1], David A. Morilak[1,4], Jun Hee Kim[2,6], Gek Ming Sia[1*]

Affiliations: [1]Department of Pharmacology, [2]Department of Cellular and Integrative Physiology, [3]Long School of Medicine, University of Texas Health at San Antonio, San Antonio, TX 78229, [4]South Texas Veteran's Health Care System, San Antonio, TX 78229, [5]University of Rochester, Rochester, NY 14627, [6]Kresge Hearing Research Institute, University of Michigan, Ann Arbor, MI 48109

*Correspondence to siag@uthscsa.edu

Summary

Microglia play a pivotal role in mediating the neurological effects of chronic stress, and is implicated in stress-associated diseases such as depression. However, the biological states of microglia in the stressed brain remains unclear. Here, using single cell RNA sequencing of mouse cortical microglia, we identify a stress-associated microglia state marked by high expression of apolipoprotein E (ApoE). In the prefrontal cortex, ApoE^{high} microglia are localized to layer 2/3, and are caused by stress-induced local complement activation in the upper cortical layers. In mice lacking complement component C3, chronic stress does not induce the ApoE^{high} microglial state, and these mice are protected from stress-induced synapse loss, anhedonia, and working memory deficits. Our data show that spatially-restricted complement and microglia activation can result in regional vulnerability of synapses in brain disease, and highlight the role of immune processes in causing region-specific circuit defects that are associated with many psychiatric diseases.

Introduction

Stress is a major risk factor for many neuropsychiatric and neurodegenerative disorders. Extended periods of psychological stress can directly lead to affective disorders such as major depressive disorder (MDD)[1], post-traumatic stress disorder (PTSD)[2,3], and anxiety disorders[2,3]. Stress also accelerates aging and the progression of neurodegenerative diseases such as Alzheimer's disease (AD)[4–6]. Lastly, stress can also trigger episodic psychiatric and neurological diseases, such as schizophrenia[7,8] and multiple sclerosis[9]. Glucocorticoid stress hormones play a critical role in the maladaptive changes caused by chronic and repeated stress. Excessive secretion of cortisol is found in 50% of depressed patients[10], and levels of cortisol are positively correlated to depressive behavior in non-human primates[11]. In humans, elevated salivary, hair and serum cortisol levels are all correlated with poorer working memory performance and lower brain volumes[12–15], suggesting that prolonged exposure to cortisol can lead to changes in brain structure. Patients with MDD also show volume reductions and synapse loss particularly in the prefrontal cortex[16–18]. In rodents, the glucocorticoid hormone corticosterone is both necessary and sufficient for stress-induced synapse loss and behavioral deficits[19,20]. Chronic and repeated stress in rodents can induce synapse loss in the medial PFC (mPFC) and deficits in working memory which are blocked by a glucocorticoid receptor antagonist[21,22], and direct administration of corticosterone to rodents can cause synapse loss in the mPFC as well as mPFC-associated behavioral deficits[23–25]. Despite the relevance of stress to human health, the pathophysiological processes through which glucocorticoid hormones cause synapse loss in the brain remain elusive.

Microglia are dynamic brain-resident macrophages that constantly survey their environment and respond to a wide variety of pathological insults. Mounting evidence from both clinical and preclinical studies indicate that microglia respond to stress, and function as key mediators in causing the neurological symptoms of stress-associated diseases. Clinical research has revealed changes in microglial morphology[26] and increases in the expression of microglia-related genes[27] in the brains of depressed patients. In rodents, chronic stress has been shown to cause microglial dysfunction which contribute towards the onset of symptoms[28–31]. Microglia are also known to phagocytose synapses in various contexts, including in the developing brain[32,33], and in many neurodevelopmental[34] and neurodegenerative diseases[35,36]. Accordingly, studies have suggested that microglial phagocytosis of synapses may also play a role in stress-induced synapse loss[37–39]. Advances in single-cell technology has allowed the study of microglial transcriptomic states in both physiological[40–43] and pathological[44–46] brain conditions. These studies have established that microglia exist in multiple homeostatic and disease-associated states, depending on their environment. Intriguingly, many disease-associated microglia states show overlapping gene signatures, and it is unclear which aspects of these signatures are unique to a particular disease, and which are due to the brain's response to the stress of sickness.

Here, we used an unbiased approach to investigate the transcriptomic states of microglia in the stressed brain by performing single-cell RNA sequencing (scRNA-seq) on sorted microglia from the cortices of mice given corticosterone for 21 days. In total, we sequenced over 35,292 cells to more than 50,000 reads per cell. We identified a transcriptomic microglia state which is dramatically upregulated in the stressed brain, marked by a large increase in the expression of the ApoE gene. Surprisingly, we found that in the mPFC, the stress-associated ApoE^{high} microglia state is localized to layer 2/3, and is absent from layer 5/6. This microglia state is driven by stress-induced localized activation of the complement system in layer 2/3 but not layer 5/6 of the mPFC. Complement activation in layer 2/3 leads to microglial phagocytosis of VGlut2 synapses and synapse loss specifically in those cortical layers, while synapses in deeper mPFC layers are spared. In complement C3 knockout (KO) mice, we found that corticosterone administration no longer induces the ApoE^{high} microglia state. C3 KO mice are also resilient to stress-induced microglia phagocytosis of synapses and synapse loss, and do not exhibit stress-induced anhedonia and working memory deficits. Our data shows that chronic stress causes layer-specific complement and microglia activation in the mPFC, which drives the neurobiological and behavioral effects of chronic stress.

Results

Stress induces an ApoE^{high} microglia state enriched in endocytotic genes

To reveal the heterogeneity of microglia in the stressed brain, we subjected C57BL/6J mice to the 21-day chronic corticosterone (CORT) administration stress protocol (Figure 1A), and performed scRNA-seq on microglia isolated from their brains. We chose the chronic CORT stress protocol because 1) CORT is the principal murine stress hormone, and all rodent stress protocols cause increases in blood CORT levels[47–49], 2) CORT is both necessary and sufficient for the circuitry and behavioral effects of chronic stress in rodents[21–25], and 3) glucocorticoid receptor blockade in rodents block stress-induced microglia activation, neuronal remodeling, and behavioral deficits[22]. We validated the chronic CORT protocol by testing mice in the sucrose preference test (SPT) for anhedonia after CORT treatment. We found that sucrose preference was significantly reduced in CORT-treated mice compared to controls (Figure 1B), as has been previously described[24,50]. To isolate single cell microglia from the gray matter of mouse cortex, we used a cold mechanical dissociation protocol that was specifically optimized for the isolation of microglia with minimal *ex vivo* transcriptional alterations (Figure 1C)[40,51]. After dissociation, microglia were sorted from the single cell suspension with fluorescence activated cell sorting (FACS) based on expression of Cd45, Cd11b, and Cx3cr1. (Supplementary Figure 1). The resulting cells were processed for single cell RNA sequencing, and sequenced to a depth of more than 50,000 reads/cell. We processed 2 biological replicates each for the control and CORT conditions, for a total of 4 biological replicates. After quality control, we retained a total of 35,292 cells from all replicates for downstream analysis.

We then performed unsupervised clustering analysis on the single scRNA-seq dataset, revealing 5 clusters across all conditions and replicates (Figure 1D). We analyzed each cluster for differentially expressed genes (DEGs), and annotated each cluster with its most highly expressed DEG, with the exception of the largest cluster, which we termed the homeostatic cluster (Figure 1D). In accordance with previous reports, adult microglia are largely homogeneous and are mostly in the homeostatic state (Figures 1D, E)[40,51,52]. Chronic CORT administration dramatically increases the number of microglia in the ApoE^{high} state in both CORT biological replicates (Figures 1E, F), while decreasing the number of homeostatic microglia. Compared to the homeostatic state, the ApoE^{high} microglia state exhibits greatly increased expression of the ApoE gene, with a nearly 32-fold increase over the homeostatic state, as well as increases in the expression of several Ms4a genes (Figure 2D). Intriguingly, both ApoE and Ms4a genes are associated with AD risk[53–55], suggesting a microglia-dependent mechanism for acceleration of AD progression by stress. In addition to the homeostatic and ApoE^{high} cell clusters, we also identified several smaller cell clusters which are largely unchanged by chronic CORT administration (Figures 1E, F), many of which have already been identified in previous microglia scRNA-seq studies[51,56,57], suggesting that they are microglia states present in basal conditions. These clusters include an interferon-responsive state marked by expression of Ifitm3 and other interferon-responsive genes (Figures 2B, C)[51,57], and a chemokine-expressing state marked by Ccl4 and other chemokine expression (Figures 2B, C)[51,56]. We also identified a microglia state marked by expression of the protein kinase Prkg1, which to our knowledge has not been previously described (Figure 2B, C). All cell clusters express canonical microglial genes such as C1qa, Cx3cr1, P2ry12, and Tmem119 (Figure 2A), indicating that they are *bona fide* microglia states.

Chronic CORT administration increases the number of microglia in the ApoE^{high} state while decreasing the number of homeostatic microglia (Figures 1D, E), suggesting that CORT induces microglia to convert from the homeostatic state to the ApoE^{high} state. To identify the genes involved in this transition, we performed pseudotime trajectory analysis on the dataset. This analysis corroborated that the homeostatic population transitioned to the ApoE^{high} population along a single trajectory (Figure 2E), and that 93 genes were differentially expressed along this trajectory, including the ApoE gene (Figure 2F). We then performed gene set enrichment analysis (GSEA) on the 93 genes, which showed that genes associated with receptor mediated endocytosis were significantly enriched among these genes (Figure 2G). In addition, genes associated with negative regulation of T cell activation and antigen presentation were also differentially expressed in microglia (Figure 2G), consistent with the known immunosuppressive function of the glucocorticoids. The enrichment of genes involved in receptor mediated endocytosis suggests that ApoE^{high} microglia are primed for phagocytosis by stress.

Stress causes layer-specific microglia activation and synapse phagocytosis

Our finding that stress-associated ApoE^{high} microglia are enriched in endocytotic genes suggests that these microglia are actively undertaking phagocytosis, a core biological function of microglia. To assess microglial phagocytosis, we stained brain slices for the microglial cytoplasmic marker Iba1 and the lysosomal marker CD68. We focused on the prelimbic cortex of the mPFC (Figure 3A), a region of the brain known to be especially sensitive to the effects of stress[58]. We reconstructed high resolution 3D images of individual microglia (Figures 3B, C), and quantitated the percentage of Iba1 volume that is occupied by CD68 lysosomes (Figure 3D, E). Surprisingly, we found that the CD68 content of microglia is increased by chronic CORT administration only in layer 2/3 of the mPFC, while microglia in layer 5/6 are not affected (Figures 3D, E).

Previous studies have shown that chronic CORT administration causes synapse loss in the mPFC[23–25]. Furthermore, live imaging studies indicate that stress-induced synapse loss in the mPFC is due to an increase in the rate of synapse elimination[24,59,60], as opposed to a decrease in the rate of synapse formation, suggesting that microglial synapse phagocytosis may be involved. To assess microglial synapse phagocytosis in the mPFC of chronically stressed mice, we stained their brain slices for Iba1, CD68, and the presynaptic marker VGlut2. We chose VGlut2 because studies from our lab and others have shown that microglia preferentially phagocytose this population of synapses[32,33,61]. We quantitated the 3D colocalization of the three markers Iba1/CD68/VGlut2 as a measure of microglial synapse phagocytosis, and found that chronic CORT administration strongly increases microglial synapse phagocytosis in layer 2/3 of the mPFC, but not in layer 5/6 (Figures 3F, G).

Stress causes layer-specific synapse loss in the mPFC

To determine if the increase in microglial synapse phagocytosis leads to a decrease in synapse density in the stressed mPFC, we stained brain slices for three types of synapses: 1) thalamocortical synapses marked by colocalized VGlut2 presynaptic and PSD95 postsynaptic markers, 2) corticocortical synapses marked by colocalized VGlut1 presynaptic and PSD95 postsynaptic markers, and 3) inhibitory synapses marked by colocalized VGAT presynaptic and gephyrin postsynaptic markers. We found that chronic CORT administration results in a layer-specific reduction of VGlut2/PSD95 synapses in layer 2/3, but not layer 5 (Figures 3H, I), while the densities of VGlut1/PSD95 and VGAT/gephyrin synapses are unchanged in all cell layers (Figures 3J-M). These findings suggest that microglial synapse phagocytosis induced by chronic CORT administration specifically targets thalamocortical synapses in layer 2/3 of the mPFC, while sparing corticocortical and inhibitory synapses.

Activity of the thalamic projections to the PFC is known to be required for working memory performance, where it acts to sustain the delay-period activity of PFC neurons which are the neuronal substrates of working memory maintenance[62–64]. Chronic stress is also known to impair

thalamic inputs to the mPFC and working memory performance in mice[21,22,65]. To determine whether stress-induced loss of structural synapses in the mPFC results in a reduction of functional activation of neurons during working memory maintenance, we utilized the temporal object recognition (TOR) working memory task, which has previously been shown to be impaired by chronic stress in mice[21,22]. We assessed the number of c-fos positive neurons in the mPFC shortly after the completion of the TOR task with immunostaining, and found a significant reduction in the number of c-fos positive cells in layer 2/3 of mPFC from CORT mice, but not in layer 5/6 (Figures 3N-P). Together, these data indicate that chronic CORT causes synapse loss in the mPFC in a layer-specific and synapse subtype-specific manner.

Multiple stress protocols cause layer-specific complement activation in the mPFC

The classical complement cascade is a major signaling pathway that mediates microglial phagocytosis of synapses[32,33,66]. Complement component C3, the main effector molecule in the complement cascade, is deposited onto synapses and recognized by microglial CR3 receptors for phagocytosis[32]. Several previous studies also suggest that chronic stress can induce complement activation in the brain[38,39,67]. Accordingly, we examined whether chronic CORT causes complement activation in the mPFC by staining for C3. We found that CORT treatment causes a layer-specific increase in C3 deposition in layer 2/3 of the mPFC but not layer 5/6 (Figures 5A-D). The effects of stress on neuroimmune processes can vary depending on the stressor used[68], raising the question of whether layer-specific complement activation is a core feature of diverse stressors. In order to determine whether layer-specific complement activation also occurs in other stressors, we assessed C3 deposition in two other commonly used stress protocols, chronic restraint stress (CRS), and chronic unpredictable stress (CUS). Both of these protocols engage the fast autonomic nervous system (ANS) response, in addition to the slow hypothalamic-pituitary-adrenal (HPA) axis hormonal response that the CORT protocol mimics. Both of these protocols also provide different patterns of CORT responses. CRS is expected to cause an initial large increase in CORT levels which habituates over time, whereas CUS is designed to cause a non-habituating increase in CORT levels. Surprisingly, both CRS and CUS cause a layer-specific increase in C3 deposition similar to that found in chronic CORT administration (Figures 4A-J), despite differences in the physiological systems engaged and patterns of CORT induced by these protocols. Therefore, multiple chronic stress protocols lead to layer-specific complement activation in the mPFC, suggesting that layer-specific mPFC vulnerability is likely to be a core feature of chronic stress, and is mediated by the complement-microglia pathway.

Complement activation drives formation of ApoE^{high} microglia state

Next, we wanted to determine if layer-specific complement activation resulted in layer-specific induction of ApoE^{high} microglia in the mPFC. We mapped ApoE-expressing microglia in the mPFC, using RNAscope *in situ* hybridization (ISH) to probe for both Cx3cr1 mRNA transcripts

as a microglia marker, and ApoE transcripts as the readout. We took a semi-quantitative approach that was suggested by the manufacturer, categorizing Cx3cr1-positive microglia into bins based on their ApoE mRNA content, ranging from no expression (bin 0) to high expression (bin 4) (Figure 5A). We then characterized the bin distribution for ApoE expression in wildtype and $C3^{-/-}$ mice treated with control or CORT (Figures 5B-E). Notably, in wildtype mice treated with CORT, over 25% of all microglia in layer 2/3 are bin 4 $ApoE^{high}$ microglia, whereas less than 10% of microglia in control mice are bin 4 $ApoE^{high}$ (Figures 5B, D). This dramatic increase in $ApoE^{high}$ microglia population is not seen in layer 5 (Figures 5C, E). In addition, C3 deletion abolishes the layer-specific increase in $ApoE^{high}$ microglia (Figures 5B-E). These data suggest that complement activation drives the formation of the $ApoE^{high}$ microglia state.

Complement activation drives stress-induced synapse loss and behavioral deficits

The lack of induction of the $ApoE^{high}$ microglia state by CORT in the $C3^{-/-}$ mice may lead to a lack of stress-induced microglial and synaptic responses in these KO mice as well. To determine if this is the case, we assessed microglial phagocytosis of VGlut2 synapses and VGlut2/PSD95 synapse density in the mPFC of control and CORT-treated $C3^{-/-}$ mice (Figures 6A, B). We found that mice lacking C3 were protected against CORT-induced microglial phagocytosis of synapses and synapse loss in layer 2/3 (Figures 6C-F). These data indicate that the absence of the $ApoE^{high}$ microglia state in $C3^{-/-}$ mice is accompanied by a lack of microglial synapse phagocytosis and synapse loss in layer 2/3 of the mPFC.

Finally, we wanted to determine if C3 deletion, which leads to the rescue of stress-induced microglial and synaptic phenotypes in the mPFC, also leads to the rescue of behavioral deficits. We assessed $C3^{-/-}$ and wildtype mice in two behavioral tasks, the SPT task for anhedonia, and the TOR task for working memory (Figures 7A, B). We found that wildtype mice, but not $C3^{-/-}$ mice, were susceptible to CORT-induced anhedonia in the SPT task (Figure 7C). In addition, we found that wildtype mice but not $C3^{-/-}$ mice were susceptible to CORT-induced impairments in working memory. Specifically, we found that control-treated wildtype mice and CORT/control-treated $C3^{-/-}$ mice were able to remember objects they have recently encountered, as shown by their preferential exploration of the old and more unfamiliar object. In contrast, CORT-treated wildtype mice were not able to remember the objects, and explored both old and recent objects equally (Figures 7D, E). Therefore, our data indicate that $C3^{-/-}$ mice are resilient against stress-induced anhedonia and working memory deficits. Taken together, our findings indicate that stress-induced layer-specific complement activation in the mPFC drives the formation of a phagocytotic $ApoE^{high}$ microglia state and leads to layer-specific synapse loss and behavioral deficits.

Discussion

In this study, we identified a stress-associated microglia state marked by greatly increased expression of the ApoE gene. We show that in the stressed mPFC, ApoE^{high} microglia are localized specifically to layer 2/3, and are caused by stress-induced complement activation in the upper cortical layers. In the stressed mPFC, microglia phagocytose VGlut2 synapses specifically in layer 2/3, resulting in anhedonia and working memory deficits. Deletion of the C3 gene blocks the stress-induced ApoE^{high} microglia state and microglial phagocytosis of synapses, and rescues stress-induced synapse loss in the mPFC and behavioral deficits. Our findings highlight the role of spatially-restricted complement activation in the brain in mediating the neurological symptoms of stress-associated diseases such as depression.

Microglia are known to be highly responsive to the environment, and scRNA-seq studies have shown that microglia adopt different transcriptomic states depending on the context. Intriguingly, many microglial states found in diseases include the upregulation of the ApoE gene. Examples of ApoE-associated microglial states include the disease-associated microglia (DAMs) found in AD[44,69], human AD microglia (HAMs)[70], the microglial neurodegenerative phenotype (MGnD) found in mouse models of AD/ALS/MS[71], microglia found in peripheral nerve injury and chronic pain[72], activated response microglia (ARMs) found in aged mice and an AD mouse model[73], microglia inflamed in MS (MIMS)[74], and a microglia state associated with injury[40]. The upregulation of microglial ApoE in a wide variety of diseases suggests that ApoE upregulation is part of a generic microglial response to tissue damage. Interestingly, early studies in stress biology describe the stress response as a "general adaptation syndrome" that occurs in diverse diseases[75,76]. In this study, we show that chronic administration of the stress hormone corticosterone induces an ApoE^{high} microglia state, suggesting that the ApoE component of multiple disease-associated microglial states is a more universal core signature that is caused by the body's stress response to sickness.

The dramatic upregulation of the ApoE gene in many disease-associated microglial states make it a useful marker for the identification of these microglia states, but does not necessarily give us information about their biological functions. Previous studies suggest that ApoE^{high} microglia exhibit a phagocytic phenotype, with the precise target of phagocytosis dependent on contextual cues. For example, cerebellar microglia express high levels of ApoE and avidly phagocytose apoptotic neurons, while striatal microglia express low levels of ApoE and show low cell clearance activity[77]. White matter-associated microglia (WAMs) also show ApoE upregulation, and are involved in clearing myelin debris[42]. In the developing brain, proliferative region-associated microglia (PAMs) exhibit high ApoE expression, and phagocytose developing oligodendrocytes [52]. Microglia are also likely to be engaged in phagocytotic clearance of damaged tissue and pathogenic protein aggregates in neurodegenerative diseases such as AD[35]. Here, we show that CORT-induced ApoE^{high} microglia phagocytose synapses, driving stress-induced synapse loss and behavioral deficits. Thus, our findings support the concept that ApoE is

a core marker for phagocytotic microglia. Excessive phagocytotic activity by ApoE^{high} microglia can lead to tissue damage and aggravate disease pathology. Hence, our findings suggest that stress aggravates many psychiatric diseases through a microglia-dependent mechanism.

While microglial ApoE expression is associated with phagocytotic activity, the molecular signals that lead to ApoE upregulation in microglia is unclear. Previous studies probing the induction of ApoE^{high} microglia states have largely focused on the phagocytosis-associated receptor TREM2, and have arrived at conflicting results. Several early studies suggest that TREM2 deletion result in microglia with reduced phagocytosis activity[78,79] and blocks transition to the MGnD microglia state[71]. However, other studies have shown that deletion of TREM2 or its signaling component Syk arrests microglia in an ApoE^{high} prodromal state, suggesting that TREM2-independent induction mechanisms also exist[44,69]. The complement system is a major cue for microglial phagocytosis of synapses[32,33,66]. In the developing brain, regions which undergo a transient increase in microglia-mediated synapse elimination also show a transient increase in complement activation[32,33]. Complement activation has also been demonstrated in many psychiatric diseases, including AD[35,80,81], FTD[36], and MS[74,82,83], and it has been shown that C1q deletion blocks the formation of the MIMS microglia state[74]. Recent studies also suggest that complement activation can occur in the context of psychological stress[38,39,67]. Here we show that 3 common forms of chronic stress, CUS, CRS, and CORT, all induce a layer-specific activation of complement component C3 in the upper layers of the mPFC. We show that stress-induced complement activation leads to the formation of an ApoE^{high} microglial state in the same cell layers, leading to synapse loss in those layers. Therefore, complement signaling may represent an alternative pathway for the generation of ApoE^{high} microglial states in many contexts, and is consistent with the increased phagocytosis activity of these microglia.

Layer- or region-specific vulnerability of synapses is a feature of many psychiatric diseases. An important question in the pathogenesis of these diseases is why specific layers or regions are vulnerable to synapse loss. For example, studies in rodent models of depression consistently show that apical dendrites of layer 5 mPFC pyramidal neurons are more sensitive to stress-induced spine loss than basal dendrites[84,85]. In schizophrenia, anatomical studies of postmortem schizophrenic brains also show a consistent loss of synapses in layer 3 of the prefrontal cortex[86–89], with normal synapse densities in layers 5 and 6[89]. Interestingly, clinical studies show that schizophrenia patients often experience their first psychotic episode shortly after a stressful life event[7,8,90], and genetic studies suggest that the complement system is involved in the pathogenesis of schizophrenia[34]. Here, we show that stress can lead to complement activation specifically in layer 2/3 of the mPFC, suggesting a molecular explanation for the striking laminar specificity of synapse loss in depression and schizophrenia, as well as providing a mechanism for the role of stress in precipitating schizophrenic attacks. Our findings suggest that brain regions differ in their susceptibility to complement activation, and that spatially-restricted complement activation in the brain can account for regional synapse vulnerability. Furthermore, we show that only VGlut2 synapses in layer 2/3 mPFC are phagocytosed by microglia, while VGlut1 and VGAT synapses are spared, indicating that even within a region of complement activation,

specific microcircuits may be selectively impaired. Future work is required to delineate the signaling pathways that lead to selective activation of complement, which can be a result of upregulation of complement components or activators, or downregulation of complement inhibitors. Understanding why particular layers or regions of the brain are vulnerable to synapse loss in psychiatric diseases can help us understand the etiology of these intractable diseases.

Acknowledgements

This work is supported by the National Institute of Neurological Disorders and Stroke (NINDS) grant (R01NS112389) to G.M.S., the National Institute on Deafness and other Communication Disorders (NIDCD) grants (R01DC018797, R01DC019371) to J.H.K, the National Institute of Mental Health (NIMH) grant (R01MH053851) to D.A.M., and the NIMH grant (R21MH113899) to F.R.C.. Imaging was performed at UTHSA Optical Imaging Facility, which is supported by a grant from the NCI (P30CA54174). FACS was performed at the Flow Cytometry Shared Resource at UTHSA, which is supported by an NCI grant (P30CA054174) to the Mays Cancer Center, a Cancer Prevention and Research Institute of Texas (CPRIT) grant (RP210126), a National Institutes of Health (NIH) Shared Instrument grant (S10OD030432), and support from the Office of the Vice President for Research at UTHSA. RNA sequencing was performed at the UTHSA Genome Sequencing Facility, which is supported by an NCI grant (P30CA054174), an NIH Shared Instrument grant (S10OD030311), and a CPRIT core facility award (RP220662).

Author contributions

G.M.S. and B.M.S. designed the study. B.M.S. carried out most of the anatomical and behavioral experiments. H.T. ,H.C., and J.G. assisted with anatomical and behavioral experiments. M.W. and J.H.K. assisted with neuronal functional experiments. J.B.L. assisted with scRNA-seq analysis. D.A.M. and F.R.C. assisted with the design of the stress protocols. G.M.S. supervised the project. G.M.S. and B.M.S. wrote the manuscript.

Declaration of interests

The authors declare no competing interests.

Data availability

Single cell RNA sequencing data will be deposited at the Gene Expression Omnibus (GEO) and be publicly available upon publication. All additional data and code will be provided upon request.

Figure legends

Figure 1. Chronic CORT administration induces an ApoE^{high} microglia state.

(A) Schematic showing timeline for chronic CORT administration and sucrose preference test.

(B) Sucrose preference in control and CORT mice. Analyzed by two-tailed unpaired t-test, t(16)=4.100, ***p=0.0008, n=9 per group.

(C) Schematic of microglia single cell isolation, FACS, and single cell RNA sequencing process.

(D) UMAP plot of 35,292 microglia isolated from the cerebral cortex of control and CORT mice, 2 replicates per condition, n = 4 mice per replicate. In total, 5 clusters of microglia were identified. The largest cluster was annotated the homeostatic cluster, while other clusters were annotated by the most differentially expressed gene compared to other clusters.

(E) Proportion of cells in each cluster for all replicates of both control and CORT conditions.

(F) UMAP plots of cells from each replicate.

Figure 2. Endocytosis-associated genes are upregulated in the ApoE^{high} microglia state.

(A) UMAP plots showing expression of canonical microglial genes.

(B) UMAP plots showing expression of marker genes for the Apoe, Prkg1, Ccl4, and Ifitm3 clusters.

(C) Heat map showing the top genes that are upregulated in each cluster relative to all other clusters.

(D) Volcano plot of differentially expressed genes (DEGs) of the Apoe^{hi} cluster versus the homeostatic cluster. Genes with $\log_2$-fold change > 0.75 are labeled.

(E) Pseudotime distribution of microglia in UMAP plot, with the homeostatic cluster designated as the root of the trajectory.

(F) Expression level of the ApoE gene in pseudotime.

(G) Dot plot showing top 10 biological function GO terms identified by gene set enrichment analysis (GSEA) of DEGs from pseudotime analysis. GO terms are arranged in order of increasing adjusted p value.

Figure 3. Chronic Stress causes layer-specific microglial activation and synapse loss in mPFC.

(A) Low-magnification image depicting layers of the medial prefrontal cortex. Stained for VGlut2 (red) and DAPI (blue).

(B) Orthogonal view showing localization of lysosomal marker CD68 (red) within Iba1-positive microglia (blue).

(C) Microglial engulfment assay. Left: Representative IHC staining of Iba1-positive microglia (green) with CD68-positive lysosomes (blue) and VGlut2 (magenta), scale bar 5 µm. Right:

Corresponding 3D reconstruction, with inset highlighting engulfed VGlut2 within microglial lysosomes. Inset scale bar 1 µm.

(D) CD68 occupancy of microglia in mPFC PrL layer 2/3. Analyzed by two-tailed unpaired t-test, t(28)=2.790, **p=0.0094, n=12-18 cells from 4 mice.

(E) CD68 occupancy of microglia in mPFC PrL layer 5. Analyzed by two-tailed unpaired t-test, t(18)=0.8727, p=0.3943, n=8-12 cells from 3-4 mice. All data shown as means ± s.e.m..

(F) VGlut2 engulfment by microglia in mPFC PrL layer 2/3. Analyzed by two-way ANOVA, followed by Sidak's post-hoc test comparing means within genotype, F(1,44)=6.067, p=0.0178, n=12-18 cells from 4 mice, ***p=0.0006. Data excerpted from wildtype groups in Figure 6D.

(G) VGlut2 engulfment by microglia in mPFC PrL layer 5. Analyzed by two-way ANOVA, F(1,31)=0.6694, p=0.4094, n=8-12 cells from 3-4 mice. All data shown as means ± s.e.m. Data excerpted from wildtype groups in Figure 6F.

(H) VGlut2/PSD95 synapse density in layer 2/3 mPFC. Representative images (left) and quantitation (right) of colocalized VGlut2 (magenta) and PSD95 (green) puncta. Circles indicate colocalized pre- and post-synaptic puncta. Scale bar 5 µm. All data shown as mean ± s.e.m. Analyzed by two-way ANOVA, followed by Sidak's post-hoc test comparing means within genotype, F(1,24)=10.67, p=0.0033 (genotype x stress interaction), n=7 from 3 mice, **p=0.0043. Data excerpted from wildtype groups in Figures 6C, E.

(I) VGlut2/PSD95 synapse density in layer 5 mPFC. Analyzed by two-way ANOVA, F(1,21)=0.07829, p=0.7824, n=6-7 from 3 mice. Data excerpted from wildtype groups in Figures 6C, E.

(J) VGlut1/PSD95 synapse density in layer 2/3 mPFC. Representative images (left) and quantitation (right) of colocalized VGlut1 (magenta) and PSD95 (green) puncta. Circles indicate colocalized pre- and post-synaptic puncta. Scale bar 5 µm. All data shown as mean ± s.e.m. Analyzed by two-tailed unpaired t-test, t(12)=0.5547, p=0.5893, n=7 from 3 mice.

(K) VGlut1/PSD95 synapse density in layer 5 mPFC. Analyzed by two-tailed unpaired t-test, t(10)=0.1575, p=0.8780, n=6 from 3 mice.

(L) VGAT/gephyrin synapse density in layer 2/3 mPFC. Representative images (left) and quantitation (right) of colocalized VGAT (magenta) and gephyrin (green) puncta. Circles indicate colocalized pre- and post-synaptic puncta. Scale bar 5 µm. All data shown as mean ± s.e.m. Analyzed by two-tailed unpaired t-test, t(9)=0.01659, p=0.9871, n=5-6 from 3 mice.

(M) VGAT/gephyrin synapse density in layer 5 mPFC. Analyzed by two-tailed unpaired t-test, t(7)=0.4156, p=0.6901, n=4-5 from 2-3 mice.

(N) Representative low-magnification image of c-fos (red) and DAPI (blue) staining in mPFC after TOR working memory task. Scale bar 50 µm.

(O) Quantitation of c-fos-positive neurons in layer 2/3 mPFC after TOR task. Analyzed by two-tailed unpaired t-test, t(30)=2.371, *p=0.0244, n=14-18 from 3-4 mice. Data shown as mean ± s.e.m.

(P) Quantitation of c-fos-positive neurons in layer 5 mPFC after TOR task. Analyzed by two-tailed unpaired t-test, t(30)=0.6996, p=0.4896, n=14-18 from 3-4 mice. Data shown as mean ± s.e.m.

Figure 4. Multiple stress protocols cause layer-specific complement activation in the mPFC.

(A) Schematic depicting timeline for chronic corticosterone (CORT) stress, chronic restraint stress (CRS), and chronic unpredictable stress (CUS) protocols.

(B) Low magnification image showing laminar C3 deposition in mPFC in control/CORT mice. Top panel shows C3 channel (white), bottom panel shows merged C3 (red) and DAPI (blue) channels. Scale bar 50 µm.

(C) Quantitation (left) and representative image (right) of C3 deposition in layer 2/3 mPFC after control/CORT. Analyzed by two-tailed unpaired t-test, t(13)=2.394, *p=0.0325, n=7-8 from 3-4 mice. All data shown as mean ± s.e.m.. Scale bar 5 µm.

(D) Quantitation (left) and representative image (right) of C3 deposition in layer 5 mPFC after control/CORT. Analyzed by two-tailed unpaired t-test, t t(14)=0.6462, p=0.5286, n=8 from 4 mice. All data shown as mean ± s.e.m.. Scale bar 5 µm.

(E) Low magnification image showing laminar C3 deposition in mPFC in control/CRS mice. Top panel shows C3 channel (white), bottom panel shows merged C3 (red) and DAPI (blue) channels. Scale bar 50 µm.

(F) Quantitation (left) and representative image (right) of C3 deposition in layer 2/3 mPFC after control/CRS. Analyzed by two-tailed unpaired t-test, t(5)=5.491, **p=0.0027, n=3-4 mice. All data shown as mean ± s.e.m.. Scale bar 5 µm.

(G) Quantitation (left) and representative image (right) of C3 deposition in layer 5 mPFC after control/CRS. Analyzed by two-tailed unpaired t-test, t(5)=0.7149, p=0.5066, n=3-4 mice. All data shown as mean ± s.e.m.. Scale bar 5 µm.

(H) Low magnification image showing laminar C3 deposition in mPFC in control/CUS mice. Top panel shows C3 channel (white), bottom panel shows merged C3 (red) and DAPI (blue) channels. Scale bar 50 µm.

(I) Quantitation (left) and representative image (right) of C3 deposition in layer 2/3 mPFC after control/CUS. Analyzed by two-tailed unpaired t-test, t(8)=2.675, *p=0.0281, n=5 from 3 mice. All data shown as mean ± s.e.m.. Scale bar 5 µm.

(J) Quantitation (left) and representative image (right) of C3 deposition in layer 5 mPFC after control/CUS. Analyzed by two-tailed unpaired t-test, t(8)=0.9416, p=0.3739, n=5 from 3 mice. All data shown as mean ± s.e.m.. Scale bar 5 µm

Figure 5. Complement activation drives formation of ApoE^{high} microglia state.

(A) Semi-quantitative scoring of RNAscope *in situ* hybridization for ApoE mRNA (red) expression in Cx3cr1-positive microglia (green). Representative images of microglia categorized into bins (0-4) based on the number of ApoE puncta/clusters per nuclei.

(B) Stacked bar graph showing ApoE bin distribution of microglia in layer 2/3 mPFC in WT and C3$^{-/-}$ control and CORT mice, displayed as % of total cells in bin; 67-85 total cells per group from 2-3 mice per group.

(C) Stacked bar graph showing ApoE bin distribution of microglia in layer 5/6 mPFC in WT and $C3^{-/-}$ control and CORT mice, displayed as % of total cells in bin; 58-85 total cells per group from 2-3 mice per group.

(D) Bar graph showing percentage of microglia within each ApoE bin category for each genotype in layer 2/3.

(E) Bar graph showing percentage of microglia within each ApoE bin category for each genotype in layer 5/6.

Figure 6. $C3^{-/-}$ mice are protected from stress-induced synapse loss.

(A) Representative images of VGlut2 (magenta) and PSD95 (green) synapses colocalization in layer 2/3 mPFC from wildtype and $C3^{-/-}$ control/CORT mice. Circles indicate colocalized pre- and postsynaptic puncta. Scale bar 5 µm.

(B) Representative images of microglial VGlut2 synapse engulfment in layer 2/3 mPFC from wildtype and $C3^{-/-}$ control/CORT mice. Representative IHC image (left) with corresponding 3D reconstruction (inset, right) showing localization of engulfed VGlut2 (magenta) in CD68-positive lysosomes (blue) in Iba1-positive microglia (green). Scale bar 5 µm for IHC image, scale bar 1 µm for inset.

(C) Quantitation of colocalized VGlut2 & PSD95 synaptic puncta in layer 2/3 mPFC of wildtype and $C3^{-/-}$ control/CORT mice. Data analyzed by two-way ANOVA, followed by Sidak's post-hoc test comparing means within genotype. $F(1,24)=10.67$, $p=0.0033$ (genotype x stress interaction), n=7 from 3 mice, **p=0.0043. Data plotted as mean ± s.e.m.

(D) Quantitation of microglial VGlut2 engulfment in layer 2/3 mPFC of wildtype and $C3^{-/-}$ mice. Data analyzed by two-way ANOVA, followed by Sidak's post-hoc test comparing means within genotype, $F(1,44)=6.067$, $p=0.0178$ (genotype x stress interaction), n=12-18 cells from 4 mice, ***p=0.0006. Data plotted as mean ± s.e.m.

(E) Quantitation of colocalized VGlut2 & PSD95 synaptic puncta in layer 5 mPFC of wildtype and $C3^{-/-}$ control/CORT mice. Data analyzed by two-way ANOVA, $F(1,21)=0.07829$, $p=0.7824$, n=6-7 from 3 mice. Data plotted as mean ± s.e.m.

(F) Quantitation of microglial VGlut2 engulfment in layer 5 mPFC of wildtype and $C3^{-/-}$ mice. Data analyzed by two-way ANOVA, $F(1,31)=0.6694$, $p=0.4094$, n=8-12 cells from 3-4 mice. Data plotted as mean ± s.e.m.

Figure 7. $C3^{-/-}$ mice are protected from stress-induced behavioral deficits.

(A) Timeline of CORT administration and behavioral assays (temporal object recognition "TOR" and sucrose preference test "SPT").

(B) Schematic diagram of TOR assay (left), with image of 3D printed objects used for assay (right).

(C) Quantitation of sucrose preference of wildtype and $C3^{-/-}$ control/CORT mice. Analyzed by two-way ANOVA, followed by Sidak's post-hoc test comparing means within genotype,

F(1,52)=4.481, p=0.0391 (genotype x stress interaction), n=12-17 per group, wildtype control vs. wildtype CORT **p=0.0017, $C3^{-/-}$ control vs. $C3^{-/-}$ CORT p=0.9298. Data plotted as mean ± s.e.m.

(D) Object exploration time during test phase of TOR. Data analyzed by three-way ANOVA, followed by uncorrected Fisher's LSD test, F(1,100)=5.758, p=0.0183 (object x genotype x stress interaction), n=25-27 per group, adjusted p-values: wildtype control old vs. wildtype control recent **p=0.0018, wildtype CORT old vs. wildtype CORT recent p=0.8376, $C3^{-/-}$ control old vs. $C3^{-/-}$ control recent *p=0.0116, $C3^{-/-}$ CORT old vs. $C3^{-/-}$ CORT recent ***p=0.0004. Data plotted as mean ± s.e.m.

(E) Bar graphs showing discrimination index of wildtype and $C3^{-/-}$ control/CORT mice, quantifying relative preference for the old object. Analyzed by two-way ANOVA, followed by Sidak's post-hoc test comparing means within genotype, F(1,100)=5.784, p=0.0180 (genotype x stress interaction), n=25-27 per group, wildtype control vs. wildtype CORT *p=0.0167, $C3^{-/-}$ control vs. $C3^{-/-}$ CORT p=0.7820.

Supplemental Figure 1. FACS gating strategy for microglia isolation before scRNA sequencing.

(A) Representative FACS plot of input cell suspension, and separation of cells from debris based on forward and side scatter.

(B) Representative FACS plot for isolation of single cells based on side scatter.

(C) Representative FACS plot for isolation of single cells based on forward scatter.

(D) Representative FACS plot for isolation of live cells based on low DAPI staining.

(E) Representative FACS plot for isolation of $CD45^{high}$ microglia cells.

(F) Representative FACS plot for isolation of $Cx3cr1^{high}$ and $Cd11b^{high}$ microglia cells.

STAR Methods

KEY RESOURCES TABLE

REAGENT or RESOURCE	SOURCE	IDENTIFIER
Antibodies		
PE anti-mouse/human CD11b (M1/70)	Biolegend	cat#: 101207, RRID:AB_312790
APC/Cyanine7 anti-mouse CD45 Antibody	Biolegend	cat#: 103115, RRID:AB_312980
APC/Anti-mouse CX3CR1 Monoclonal Antibody [clone: SA011F11]	Biolegend	cat#: 149007, RRID:AB_2564491
Rabbit anti-Iba1	Fuji Film	cat#: 019-19741, RRID:AB_839504
Rat anti-CD68	Bio-Rad	cat#: MCA1957, RRID:AB_322219
Guinea pig anti-VGlut2	Synaptic Systems	cat#: 135 404, RRID:AB_887884
Rabbit anti-VGlut1	Synaptic Systems	cat#: 135 302, RRID:AB_887877
Mouse anti-PSD95 K28/43, IgG2a	Neuromab	cat#: 75-028, RRID:AB_2292909
Guinea pig anti-VGAT	Synaptic Systems	cat#: 131 004, RRID:AB_887873
Mouse anti-gephyrin, IgG1	Synaptic Systems	cat#: 147 021, RRID:AB_2232546
Rabbit anti-cFOS	Synaptic Systems	cat#: 226-008, RRID:AB_2891278
Donkey Anti-Goat IgG Antibody (Alexa Fluor® 488)	Jackson ImmunoResearch	cat#: 705-545-147, RRID:AB_2336933
Goat anti-C3	MP Biomedicals	cat#: 855730
Donkey Anti-Rabbit IgG Antibody (Alexa Fluor® 488)	Jackson ImmunoResearch	cat#: 711-545-152, RRID:AB_2313584
Cy3-AffiniPure Donkey Anti-Rat IgG (H+L)	Jackson ImmunoResearch	cat#: 712-165-153, RRID:AB_2340667
Goat Anti-Guinea Pig IgG Polyclonal Antibody (CF™ 488A)	Biotium	cat#: 20017-1, RRID:AB_10854842
Cy5-AffiniPure Donkey Anti-Guinea Pig IgG (H+L)	Jackson ImmunoResearch	cat#: 706-175-148, RRID:AB_2340462
Goat Anti-Rabbit IgG H&L (Cy5 ®)	Abcam	cat#: ab6564, RRID:AB_955061

Goat anti-Mouse IgG2a Secondary Antibody, Alexa Fluor 555	Thermo Fisher Scientific	cat#: A-21137, RRID:AB_2535776
Goat anti Guinea Pig IgG (H+L) Secondary Antibody, Alexa Fluor 647	Thermo Fisher Scientific	cat#: A-21450, RRID:AB_141882
Goat anti-Mouse IgG1 Secondary Antibody, Alexa Fluor® 488	Thermo Fisher Scientific	cat#: A-21121, RRID:AB_2535764
Chemicals, Peptides, and Recombinant Proteins		
DAPI	Thermo Fisher Scientific	cat#: D1306
Corticosterone	Millipore Sigma	cat#: 27840-500MG
Hanks Balanced Salt Solution, no calcium, magnesium or phenol red	Gibco	cat#: 14175095
Percoll	Sigma-Aldrich	cat#: P1644-100ML
Fc block reagent	BD Biosciences	cat#: 553141
Opal 520	Akoya	cat#: FP1487001KT
Opal 570	Akoya	cat#: FP1488001KT
Normal Donkey Serum	Jackson ImmunoResearch	cat#: 017-000-121
Normal Goat Serum	Jackson ImmunoResearch	cat#: 005-000-121
TrueBlack Lipofuscin Autofluorescence Quencher	Biotium	cat#: 23007
Fluoromount-G	SouthernBiotech	cat#: 0100-01
Critical Commercial Assays		
Chromium 3' library v3.1 kit	10x Genomics	PN-1000269
RNAscope Multiplex Fluorescent V2 Assay	ACD Bio	cat#: 323136
ApoE-C3 Probe	ACD Bio	cat#: 313271-C3
CX3CR1-C2 Probe	ACD Bio	cat#: 314221-C2
Experimental Models: Organisms/Strains		
Mouse: WT: C57BL/6	Jackson Laboratory; Bred in-house	IMSR_JAX:000664
Mouse: $C3^{-/-}$:B6.129S4-*C3*^{tm1Crr}/J	Jackson Laboratory; Bred in-house	IMSR_JAX:029661
Software and Algorithms		
GraphPad Prism	Dotmatics	Version 9; RRID:SCR_002798
Cell Ranger	10x Genomics	Version 7.0.1
R Studio	https://www.rstudio.com/	2022.02.3 Build 492
R	https://www.r-project.org/	Version 4.2.1
Seurat	https://satijalab.org/seurat/	Version 4.3.0
DoubletFinder	https://github.com/chris-mcginnis-ucsf/DoubletFinder	Version 2.0.3
EnhancedVolcano	https://github.com/kevinblighe/EnhancedVolcano	Version 1.14.0
Monocle3	https://cole-trapnell-lab.github.io/monocle3/	Version 1.3.1
clusterProfiler	https://guangchuangyu.github.io/software/clusterProfiler/	Version 4.4.4

Imaris	Bitplane	Version 9.7.1; RRID:SCR_007370
ImageJ	NIH	Version 1.53q; RRID:SCR_003070
Ethovision	Noldus	Version 11.5.1024; RRID:SCR_000441
Other		
Dounce homogenizer - 7 mL	Bellco Glass, Inc.	cat#: 198410007
Low-aldehyde falcon tubes	StellarScientific	cat#: T50-600
Sipper Tubes	Fisher Scientific	cat#: NC1636707
Rubber Stoppers	VWR	cat#: 76293-684
Red Biotunnel	Bioserv	cat#: K3322
Open Field, Mouse, Set of 4	Conduct Science	n/a

Animal care

All animal work was approved by the UT Health Institutional Animal Care and Use Committee (IACUC). Colonies were maintained in climate-controlled rooms within the AAALAC-accredited UT Health animal facility. Mice were group-housed (3-4 per cage) under a 14-hour light/10-hour dark cycle with ad libitum access to food and water. Clear red-tinted tunnels (Bioserv, K3322) were placed in all cages for enrichment and transport purposes. To reduce distress during transfer, mice were habituated to tunnel handling with daily 3-5 min tube rides for 1 week prior to behavioral studies. Behavioral assays were conducted either during the last 4 hours of the light cycle (temporal object recognition) or throughout the dark cycle (sucrose preference test).

Chronic corticosterone (CORT) stress protocol

Mice received either corticosterone-infused (CORT) drinking water (Sigma 27840, corticosterone dissolved at 10 mg/ml in 100% ethanol, then mixed with facility-provided drinking water to a final concentration of 0.1 mg/ml corticosterone and 1% ethanol) or control drinking water (1% ethanol) for 21 days, as described[24]. Both CORT and control water were prepared in standard bottles using autoclaved drinking water from the animal facility and replaced weekly.

Chronic restraint stress (CRS) protocol

Mice were subjected to 4 hours of restraint stress daily for 21 days, as described[24]. Restraint tubes were made from 50 mL canonical tubes (Falcon, #2098) with drilled holes for air circulation. Restraint tubes were placed inside the home cage. Control mice were handled twice

daily, 4 hours apart, for 5 minutes each. Tubes were cleaned with 70% ethanol between uses.

Chronic unpredictable stress (CUS) protocol

We used a protocol that had been shown in multiple studies to cause stress-induced circuitry changes in mice[91,92]. Mice were subjected to two different stressors per day, once in the morning and once in the afternoon, for 10 days. Stressors included: 15 min tail pinch, 2 hr tube restraint, 30 min elevated platform, 10 min inescapable footshock (0.7mA, 2 s, 10 total shocks), 24 hr wet bedding with 45° cage tilt, and 24 hr light exposure. Control mice were handled twice daily. CUS mice were singly housed for the duration of the stress protocol, while control mice were group housed.

Microglia single cell dissociation and FACS

Microglia single cell dissociation was performed using the cold mechanical dissociation procedure which minimizes ex vivo activation of microglia as previously described[40,51]. Brains were collected from control and CORT mice after transcardiac perfusion of ice-cold HBSS, and the cerebral cortices were dissected out and minced after removal of white matter. Pieces of cortices were then Dounce homogenized for 20 strokes with a loose rotating pestle, and then strained through a 70 µm strainer. Cells were washed and pelleted in HBSS, and then resuspended in 40% Percoll. Cells were spun at 500 g in the cold for 1 hr, and the pelleted cells were washed in HBSS and resuspended in FACS buffer for staining. Cell suspensions were incubated with Fc block reagent (1:50 dilution) for 15 min on ice, and then the following antibodies were added from a master mix: DAPI (1:10,000), Cd11b-PE (1:50), CD45-APC-Cy7 (1:100), Cx3cr1-APC (1:250). Cell suspensions were further incubated for 30 min on ice, and then washed twice and resuspended in FACS buffer. Cells were then immediately transported to the Flow Cytometry Core Facility on ice for sorting. Sorting was performed with the following gating strategy (Supplementary Figure 1): whole cells versus debris (forward scatter (FSC-A) vs side scatter (SSC-A)), singlets vs aggregates (SSC-H vs SSC-A, and FSC-H vs FSC-A), live vs dead (DAPI vs SSC-A), $Cd45^{high}$ (APC-Cy7-CD45 vs SSC-A), $Cx3cr1^{high}$ and $Cd11b^{high}$ (APC-CX3CR1 vs PE-CD11b).

Single cell library generation and sequencing

After sorting in the cold, cells were put on ice and immediately transported to the Genome Sequencing Core Facility for 10X Genomics single-cell capture and sequencing with the Chromium 3' library v3.1 kit, following manufacturer's instructions. Approximately 10,000 cells were targeted per sample for single cell sequencing. The single cell libraries were then sequenced on an Illumina NovaSeq6000 sequencer, targeting at least 500M reads per sample, for an average sequencing depth of 50,000 reads per cells. Cell Ranger v7.0.1 (10X Genomics) was used for sample demultiplexing, barcode processing, unique molecular identifiers filtering, gene counting, and mapping to the mouse mm10-2020-A (10X Genomics) reference genome.

scRNA-seq clustering analysis

Single cell clustering analysis was performed with the R package Seurat v4.3.0[93]. For initial quality filtering, genes expressed in more than 5 cells were kept. Cells with greater than 5% mitochondrial gene expression or less than 2% ribosomal gene expression were then removed. Lastly, cells expressing more than 2000 genes and 5000 UMIs were kept. The SCTransform v2 algorithm[94] from Seurat was then used to normalize the counts in each sample. Cells were then filtered for doublets using the R package DoubletFinder[95], based on an expected doublet rate of 7.6% for 10,000 cells per channel, as specified in the manufacturer's instructions. After filtering, a total of 35,292 microglia were retained for downstream analysis.

Cells from all samples were integrated with Canonical Correlation Analysis (CCA) with Seurat's *SelectIntegrationFeatures*, *PrepSCTIntegration*, *FindIntegrationAnchors*, and *IntegrateData* functions. Principal Components Analysis (PCA) was then performed for the integrated dataset, and the top 20 principal components (PCs) were chosen for clustering based on an elbowplot. Clustering was performed using the *FindNeighbors* function with 20 PCs, and the *FindClusters* function at a resolution of 0.08. Uniform Approximation and Projection (UMAP) dimensionality reduction was performed to visualize the cell clusters with the *RunUMAP* and *DimPlot* functions. Marker genes for clusters were identified using the *FindAllMarkers* function with the Wilcoxon rank-sum test. The top expressing genes in each cell cluster was plotted as a heat map using the *DoHeatMap* function. Comparison of differentially expressed genes (DEGs) between the homeostatic and ApoE^{high} clusters were performed with the *FindMarkers* function with the parameter max.cells.per.ident = 3000, and the results were plotted in a volcano plot using the EnhancedVolcano R package[96].

Pseudotime trajectory analysis

The R package Monocle3[97] was used to construct a pseudotime trajectory in the clustered dataset and to identify genes that were differentially expressed along the pseudotime trajectory. The *learn_graph* function of Monocle3 was used to fit a principal graph in the combined dataset, and the *order_cells* function was used to order the cells into trajectory along the principal graph, with graph nodes in the homeostatic cluster specified as the root of the trajectory. Genes that were differentially expressed along the pseudotime trajectory were determined using the *graph_test* function.

Gene set enrichment analysis (GSEA)

The R package clusterProfiler[98] was used to perform GSEA. The list of DEGs from the pseudotime trajectory analysis (log2FC > 0.25 and adjusted p value < 0.05, resulting in a total of 93 genes) was used as input to the *enrichGO* function of clusterProfiler with the following

parameters: keyType = "SYMBOL", OrgDb = org.Mm.eg.db, ont = "BP", pvalueCutoff = 0.05, pAdjustMethod = "BH". The top 10 enriched biological process (BP) gene ontology (GO) terms were ranked in order of increasing adjusted p value, and plotted as a dot plot.

Immunohistochemistry and microscopy

Mice were deeply anesthetized with Avertin (0.5 mg/g) for transcardial perfusion with ice-cold PBS and 4% paraformaldehyde (PFA). Brains were rapidly extracted, post-fixed for 2 hrs at 4°C with gentle rocking, then cryoprotected in 30% sucrose in PBS for 48-72 hours. Brains were sliced on a sliding-freezing microtome (Leica) into 20 µm sections (for synapse and complement staining) or thick 40 µm sections (for microglia staining). Wash, block and antibody solutions were made from PBS (pH 7.4) with either 0.15% TX-100 (0.15% PBT) or 0.3% PBT, depending on slice thickness. Free-floating sections were washed 2x in PBT (10 min/wash), post-fixed in 4% PFA (15min) and briefly rinsed in PBS (5 min) while rocking at room temperature (RT). Sections were blocked in 10% normal donkey/goat serum (Jackson Immunoresearch) at RT for 2 hr, then incubated in primary antibodies in 1% blocking buffer overnight at 4°C with gentle rocking. Once equilibrated to RT, sections were washed 4x (10 min/wash), then incubated in secondary for 2 hr. Sections were washed 2x in PBT (5 min/wash), 3x in PBS (10 min/wash) then floated onto glass slides. Slides were treated with TrueBlack Lipofuscin Autofluorescence Quencher (Biotium, 23007), rinsed 3x in PBS (3min/wash), then cover-slipped with Fluoromount-G (SouthernBiotech, 0100-01). Slides were stored in 4° and imaged within 1 week.

The following primary antibodies were used for staining: goat anti-C3 (1:1000, MP Biomedicals, cat#: 855730), rabbit anti-Iba1 (1:500, Fuji Film, cat#: 019-19741), rat anti-CD68 (1:500, Bio-Rad, cat#: MCA1957), guinea pig anti-VGlut2 (1:1000, Synaptic Systems, cat#: 135 404), rabbit anti-VGlut1 (1:1000, Synaptic Systems, cat#: 135 302), mouse anti-PSD95 K28/43, IgG2a (1:500, Neuromab, cat#: 75-028), guinea pig anti-VGAT (1:500, Synaptic Systems, cat#: 131 004), mouse anti-gephyrin, IgG1 (1:500, Synaptic systems, cat#: 147 021), rabbit anti-cFOS (1:500, Synaptic systems, cat#: 226-008).

The following secondary antibodies were used for staining: donkey Anti-Goat IgG A488 (1:500, Jackson, cat#: 705-545-147), donkey Anti-Rabbit IgG A488 (1:500, Jackson, cat#: 711-545-152), cy3-AffiniPure Donkey Anti-Rat IgG H&L (1:500, Jackson, cat#: 712-165-153), goat Anti-Guinea Pig IgG Polyclonal CF-488A (1:500, Biotium, cat#: 20017-1), cy5-AffiniPure Donkey Anti-Guinea Pig IgG H&L (1:500, Jackson, cat#: 706-175-148), goat Anti-Rabbit IgG H&L Cy5 (1:500, Abcam, cat#: ab6564), goat anti-Mouse IgG2a A555 (1:500, Thermo Fisher Scientific, cat#: A-21137), goat anti Guinea Pig IgG H&L A647 (1:500, Thermo Fisher Scientific, cat#: A-21450), goat anti-Mouse IgG1 A488 (1:500, Thermo Fisher Scientific, cat#: A-21121).

Sections were imaged using a Zeiss AxioObserver inverted microscope equipped with a Zeiss Apotome.2 module. Images were acquired using a Zeiss 63x/1.4 oil Plan-Apochromat objective

(synapse density, microglial activation and engulfment, high-resolution C3), or Zeiss 20x Plan-Neofluar objective (low-magnification C3 staining). Identical imaging and analysis parameters were used for each experimental group.

Image analysis for C3 deposition and synapse densities

ImageJ (NIH) was used to quantify synapse densities and C3 deposition. Individual channels were first Z-projected with summation over a depth of 2 µm, followed by background subtraction (8 px rolling ball radius) and gaussian filter (sigma = 0.8). The threshold was empirically determined for each channel and applied consistently to all groups. Watershed was applied to binarized image. For synapse density, colocalized puncta were revealed by multiplying the individual pre & post-synaptic channels using the image calculator tool. The Analyze Particles tool was used to quantify the number of colocalized synaptic puncta and individual C3 deposits.

Image analysis for microglial lysosome content and synapse phagocytosis

Reconstructions of microglia were performed using high-resolution confocal-quality images of Iba1-positive cells using Imaris Software (version 9.7.1, Bitplane, Concord MA), as previously described[32,33]. Using the image processing tool, background subtraction was first performed (sigma = 1 for VGlut2, CD68; sigma = 60 for Iba1), followed by the application of a gaussian filter (sigma = 0.144). All surfaces were rendered with 0.1 µm smoothing. Iba1-positive cells were reconstructed first, and disconnected processes were unified with the cell body to create a single surface representing one cell. To render CD68, a mask was then applied to isolate the CD68 signal only within the reconstructed microglia. Another mask was then applied to isolate the VGlut2 signal only within the reconstructed CD68-positive lysosomes within microglia. Volumes were recorded for each reconstructed surface. For microglial lysosome content, the percent of CD68 occupancy within microglia was calculated using the formula: *(volume of CD68/volume of Iba1+ cell)*100*. For microglial engulfment of VGlut2, the percent of VGlut2 within microglial lysosomes was calculated using the formula: *(volume of VGlut2 within lysosome/volume of Iba1+ cell)*100*.

Quantification of c-fos positive cells

Mice were sacrificed exactly 1 hour after completion of the TOR test phase. Brain tissue was collected and processed as described above with slight modifications. In short, 40 µm-thick brain sections were fixed in ice-cold 100% methanol for 5 minutes, washed in 0.3% PBT for 15 minutes, then blocked in 1% BSA 5% NDS in 0.3% PBT for 2 hours at RT. Sections were incubated in primary antibody in blocking buffer overnight (rabbit anti-c-fos, 1:1000, Synaptic Systems 226-008), washed 5x with PBT, then incubated in secondary antibody (donkey anti-

rabbit A488, Jackson, catalog #: 711-545-152) for 2 hr at RT. Sections were imaged on a Zeiss AxioObserver inverted microscope equipped with Apotome.2 module using a Zeiss 20x Plan-Neofluar objective. Analysis of c-fos positive cells was automated using an ImageJ macro by applying the following sequence on 200 µm x 200 µm ROIs: gaussian filter (sigma = 2), threshold (1000,65535), convert to binary mask, watershed, analyze particles.

RNAscope ISH

RNAscope™ Multiplex Fluorescent V2 assay (ACDBio, 323136) was carried out according to manufacturer's instructions, with small modifications. Briefly, brains from PBS-perfused mice were rapidly dissected and snap frozen in liquid nitrogen. Brains were sliced using a cryostat into 16um sections and adhered onto super-frost plus slides (Electron Microscopy Sciences, 71869-20). Slides were kept on dry ice during slicing and then promptly stored at -80°C in a sealed box until use. Immediately upon removal from the freezer, slides were plunged into fresh ice-cold 4% PFA for 15 min, rinsed 2x with PBS, then dehydrated in serial dilutions of ethanol (50%, 75%, 100%, 100%). Slides were then air-dried for 5 min, and a PAP pen was used to create a hydrophobic barrier around the tissue. For all subsequent steps, slides were moved to the HybEZ Humidity Control Tray with wet humidifying paper for treatment/incubation, and washed in coplin jars with gentle rocking (2 min per wash). At room temperature (RT), sections were treated with hydrogen peroxide for 10 min, washed 3x in distilled water, treated with Protease IV for 20 min, then washed 3x with PBS. Probes (Mm-CX3CR1-C2, cat no. 314221-C2 and ApoE-C3, cat no. 313271-C3) were hybridized to tissue at 37°C for 2 hr, rinsed 3x in wash buffer, and stored in 5x saline sodium citrate (5x SSC) buffer overnight at RT. Slides were rinsed 1x with wash buffer before experiment continuation. Subsequent amplification & HRP steps were performed according to manufacturer's instructions. HRP-C2 and HRP-C3 were labelled with Opal 520 (1:750, Akoya FP1487001KT) and Opal 570 (1:1500, Akoya FP1488001KT), respectively. Slides were counterstained with DAPI, cover slipped with Prolong Gold (Cell Signaling Technology #9071), stored in 4°C and imaged within 1 week.

Images were acquired with a Zeiss AxioObserver equipped with an Apotome.2 module using a Zeiss 40x Plan-Neuofluar objective. Analysis of ApoE expression was limited to CX3CR1+ DAPI nuclei. ApoE expression within microglia was evaluated using the ACDBio semi-quantitative scoring system: "0" represents no staining or less than one dot per ten cells, "1" represents one to three dots per cell, "2" represents four to nine dots per cell and none or very few dot clusters, "3" represents 10 to 15 dots per cell and/or less than 10% of dots in clusters, and "4" represents more than 15 dots per cell and/or more than 10% of dots in clusters. Bin counts were aggregated within each experimental group (N=3-4 mice per group, 1-2 images per mouse) to determine the bin distribution for each condition.

Sucrose preference test (SPT) task

Sucrose preference test was conducted using a 1% sucrose solution (Sigma S9378-1KG). Bottles were made from 50 mL conical "iTubes" with low-aldehyde odor (Stellar Scientific, T50-600) custom fitted with 2.5" sipper tubes (Fisher, NC1636707) and rubber stoppers (VWR, 76293-684) to minimize leakage. Sucrose and control water were prepared using autoclaved drinking water from the animal facility. Sucrose water and control water were sterile filtered before aliquoting into conical tubes. Mice were simultaneously habituated to sucrose and control water bottles for 3 consecutive days prior to testing. Bottles were switched in positions once daily to avoid side preference. On the test day, mice were separated into individual housing and deprived of water for the last 4 hours of the light cycle. Sucrose and water bottles were weighed at the beginning and end of the dark cycle. Percent sucrose preference was calculated with the following formula: *((sucrose consumption - water consumption) / total consumption) x 100*

Temporal Object Recognition (TOR) task

TOR was conducted in an 80 x 80 x 30 cm white acrylic open field arena, with white opaque wall inserts separating the arena into (4) 40 x 40 x 30 cm height square chambers (Conduct Science). Objects were 3D printed from natural PLA filament (3D printer files provided by Maithe Arruda-Carvalho[99]). Two types of objects were printed: steps and domes. To minimize intrinsic preference of mice for either object, both objects were made of the same material, and were designed to be equal in surface area. Objects were also tested in pilot studies to verify that mice had no intrinsic preference for either object, and counterbalanced between phase 1 and phase 2 as described below. Objects were centered midway along the inside of the external chamber walls, equidistant from the corners. To prevent movement, objects were affixed to the chamber floor using a small piece of BluTack adhesive putty (a fresh piece was used every round for every mouse). Chambers and objects were cleaned with 15% ethanol between each mouse and phase to minimize odor carryover. All equipment was cleaned with 70% ethanol at the end of the test session. Mice were habituated to each quadrant (chamber) of the arena, 5 min per chamber, for two consecutive days prior to testing. The TOR procedure consisted of three 5-minute phases (phase 1, phase 2 and test) with 1 hr inter-phase intervals. Mice were returned to home cage between phases. During phase 1, mice were placed in the arena with a pair of identical objects (either 2 steps or 2 domes). After a 1 hr delay, mice were reintroduced to the same chamber containing a different pair of identical objects for phase 2. During the test phase, mice were reintroduced to the same chamber containing one object from phase 1 (old object) and one object from phase 2 (recent object). Sessions were recorded using an infrared camera (OEM Cameras, DFK 33UX290) with a 3-8mm focal length lens (OEM Cameras, T3Z0312CS-MPIR) fixed to the ceiling directly above the arena. Videos were analyzed using Noldus Ethovision tracking software (Noldus Ethovision XT, Version 11.5). Behavioral analysis during the test phase was restricted to the first 20 s of total interaction time with objects, as previously described[99]. The object discrimination index was calculated using the following formula: *old object interaction time / total object interaction time*.

References:

1. Hammen, C. (2005). Stress and depression. Annu. Rev. Clin. Psychol. *1*, 293–319. 10.1146/annurev.clinpsy.1.102803.143938.

2. McEwen, B.S., and Akil, H. (2020). Revisiting the Stress Concept: Implications for Affective Disorders. J. Neurosci. *40*, 12–21. 10.1523/JNEUROSCI.0733-19.2019.

3. Smoller, J.W. (2016). The Genetics of Stress-Related Disorders: PTSD, Depression, and Anxiety Disorders. Neuropsychopharmacology *41*, 297–319. 10.1038/npp.2015.266.

4. Sotiropoulos, I., Catania, C., Pinto, L.G., Silva, R., Pollerberg, G.E., Takashima, A., Sousa, N., and Almeida, O.F.X. (2011). Stress Acts Cumulatively To Precipitate Alzheimer's Disease-Like Tau Pathology and Cognitive Deficits. J. Neurosci. *31*, 7840–7847. 10.1523/JNEUROSCI.0730-11.2011.

5. Harvanek, Z.M., Fogelman, N., Xu, K., and Sinha, R. (2021). Psychological and biological resilience modulates the effects of stress on epigenetic aging. Transl. Psychiatry *11*, 1–9. 10.1038/s41398-021-01735-7.

6. Madore, C., Yin, Z., Leibowitz, J., and Butovsky, O. (2020). Microglia, Lifestyle Stress, and Neurodegeneration. Immunity *52*, 222–240. 10.1016/j.immuni.2019.12.003.

7. Birley, J.L., and Brown, G.W. (1970). Crises and life changes preceding the onset or relapse of acute schizophrenia: clinical aspects. Br. J. Psychiatry J. Ment. Sci. *116*, 327–333. 10.1192/bjp.116.532.327.

8. Nuechterlein, K.H., Dawson, M.E., Ventura, J., Gitlin, M., Subotnik, K.L., Snyder, K.S., Mintz, J., and Bartzokis, G. (1994). The vulnerability/stress model of schizophrenic relapse: a longitudinal study. Acta Psychiatr. Scand. Suppl. *382*, 58–64. 10.1111/j.1600-0447.1994.tb05867.x.

9. Mohr, D.C., Hart, S.L., Julian, L., Cox, D., and Pelletier, D. (2004). Association between stressful life events and exacerbation in multiple sclerosis: a meta-analysis. BMJ *328*, 731. 10.1136/bmj.38041.724421.55.

10. Parker, K.J., Schatzberg, A.F., and Lyons, D.M. (2003). Neuroendocrine aspects of hypercortisolism in major depression. Horm. Behav. *43*, 60–66. 10.1016/s0018-506x(02)00016-8.

11. Qin, D.-D., Rizak, J., Feng, X.-L., Yang, S.-C., Lü, L.-B., Pan, L., Yin, Y., and Hu, X.-T. (2016). Prolonged secretion of cortisol as a possible mechanism underlying stress and depressive behaviour. Sci. Rep. *6*, 30187. 10.1038/srep30187.

12. Lee, B.K., Glass, T.A., McAtee, M.J., Wand, G.S., Bandeen-Roche, K., Bolla, K.I., and Schwartz, B.S. (2007). Associations of salivary cortisol with cognitive function in the Baltimore memory study. Arch. Gen. Psychiatry *64*, 810–818. 10.1001/archpsyc.64.7.810.

13. Pulopulos, M.M., Hidalgo, V., Almela, M., Puig-Perez, S., Villada, C., and Salvador, A. (2014). Hair cortisol and cognitive performance in healthy older people. Psychoneuroendocrinology *44*, 100–111. 10.1016/j.psyneuen.2014.03.002.

14. Geerlings, M.I., Sigurdsson, S., Eiriksdottir, G., Garcia, M.E., Harris, T.B., Gudnason, V., and Launer, L.J. (2015). Salivary cortisol, brain volumes, and cognition in community-dwelling elderly without dementia. Neurology *85*, 976–983. 10.1212/WNL.0000000000001931.

15. Echouffo-Tcheugui, J.B., Conner, S.C., Himali, J.J., Maillard, P., DeCarli, C.S., Beiser, A.S., Vasan, R.S., and Seshadri, S. (2018). Circulating cortisol and cognitive and structural brain measures: The Framingham Heart Study. Neurology *91*, e1961–e1970. 10.1212/WNL.0000000000006549.

16. Fries, G.R., Saldana, V.A., Finnstein, J., and Rein, T. (2023). Molecular pathways of major depressive disorder converge on the synapse. Mol. Psychiatry *28*, 284–297. 10.1038/s41380-022-01806-1.

17. Kang, H.J., Voleti, B., Hajszan, T., Rajkowska, G., Stockmeier, C.A., Licznerski, P., Lepack, A., Majik, M.S., Jeong, L.S., Banasr, M., et al. (2012). Decreased expression of synapse-related genes and loss of synapses in major depressive disorder. Nat. Med. *18*, 1413–1417. 10.1038/nm.2886.

18. Duman, R.S., and Aghajanian, G.K. (2012). Synaptic Dysfunction in Depression: Potential Therapeutic Targets. Science *338*, 68–72. 10.1126/science.1222939.

19. de Kloet, E.R., Joëls, M., and Holsboer, F. (2005). Stress and the brain: from adaptation to disease. Nat. Rev. Neurosci. *6*, 463–475. 10.1038/nrn1683.

20. Hall, B.S., Moda, R.N., and Liston, C. (2015). Glucocorticoid mechanisms of functional connectivity changes in stress-related neuropsychiatric disorders. Neurobiol. Stress *1*, 174–183. 10.1016/j.ynstr.2014.10.008.

21. Yuen, E.Y., Wei, J., Liu, W., Zhong, P., Li, X., and Yan, Z. (2012). Repeated Stress Causes Cognitive Impairment by Suppressing Glutamate Receptor Expression and Function in Prefrontal Cortex. Neuron *73*, 962–977. 10.1016/j.neuron.2011.12.033.

22. Horchar, M.J., and Wohleb, E.S. (2019). Glucocorticoid receptor antagonism prevents microglia-mediated neuronal remodeling and behavioral despair following chronic unpredictable stress. Brain. Behav. Immun. *81*, 329–340. 10.1016/j.bbi.2019.06.030.

23. Wellman, C.L. (2001). Dendritic reorganization in pyramidal neurons in medial prefrontal cortex after chronic corticosterone administration. J. Neurobiol. *49*, 245–253. 10.1002/neu.1079.

24. Moda-Sava, R.N., Murdock, M.H., Parekh, P.K., Fetcho, R.N., Huang, B.S., Huynh, T.N., Witztum, J., Shaver, D.C., Rosenthal, D.L., Alway, E.J., et al. (2019). Sustained rescue of

prefrontal circuit dysfunction by antidepressant-induced spine formation. Science *364*, eaat8078. 10.1126/science.aat8078.

25. Anderson, R.M., Glanz, R.M., Johnson, S.B., Miller, M.M., Romig-Martin, S.A., and Radley, J.J. (2016). Prolonged corticosterone exposure induces dendritic spine remodeling and attrition in the rat medial prefrontal cortex. J. Comp. Neurol. *524*, 3729–3746. 10.1002/cne.24027.

26. Torres-Platas, S.G., Cruceanu, C., Chen, G.G., Turecki, G., and Mechawar, N. (2014). Evidence for increased microglial priming and macrophage recruitment in the dorsal anterior cingulate white matter of depressed suicides. Brain. Behav. Immun. *42*, 50–59. 10.1016/j.bbi.2014.05.007.

27. Seney, M.L., Huo, Z., Cahill, K., French, L., Puralewski, R., Zhang, J., Logan, R.W., Tseng, G., Lewis, D.A., and Sibille, E. (2018). Opposite Molecular Signatures of Depression in Men and Women. Biol. Psychiatry *84*, 18–27. 10.1016/j.biopsych.2018.01.017.

28. Bollinger, J.L., and Wohleb, E.S. (2019). The formative role of microglia in stress-induced synaptic deficits and associated behavioral consequences. Neurosci. Lett. *711*, 134369. 10.1016/j.neulet.2019.134369.

29. Niraula, A., Sheridan, J.F., and Godbout, J.P. (2017). Microglia Priming with Aging and Stress. Neuropsychopharmacol. Off. Publ. Am. Coll. Neuropsychopharmacol. *42*, 318–333. 10.1038/npp.2016.185.

30. Picard, K., St-Pierre, M.-K., Vecchiarelli, H.A., Bordeleau, M., and Tremblay, M.-È. (2021). Neuroendocrine, neuroinflammatory and pathological outcomes of chronic stress: A story of microglial remodeling. Neurochem. Int. *145*, 104987. 10.1016/j.neuint.2021.104987.

31. Walkera, F.R., Nilsson, M., and Jones, K. (2013). Acute and Chronic Stress-Induced Disturbances of Microglial Plasticity, Phenotype and Function. Curr. Drug Targets *14*, 1262–1276. 10.2174/13894501113149990208.

32. Schafer, D.P., Lehrman, E.K., Kautzman, A.G., Koyama, R., Mardinly, A.R., Yamasaki, R., Ransohoff, R.M., Greenberg, M.E., Barres, B.A., and Stevens, B. (2012). Microglia sculpt postnatal neural circuits in an activity and complement-dependent manner. Neuron *74*, 691–705. 10.1016/j.neuron.2012.03.026.

33. Cong, Q., Soteros, B.M., Wollet, M., Kim, J.H., and Sia, G.-M. (2020). The endogenous neuronal complement inhibitor SRPX2 protects against complement-mediated synapse elimination during development. Nat. Neurosci. *23*, 1067–1078. 10.1038/s41593-020-0672-0.

34. Sekar, A., Bialas, A.R., de Rivera, H., Davis, A., Hammond, T.R., Kamitaki, N., Tooley, K., Presumey, J., Baum, M., Van Doren, V., et al. (2016). Schizophrenia risk from complex variation of complement component 4. Nature *530*, 177–183. 10.1038/nature16549.

35. Hong, S., Beja-Glasser, V.F., Nfonoyim, B.M., Frouin, A., Li, S., Ramakrishnan, S., Merry, K.M., Shi, Q., Rosenthal, A., Barres, B.A., et al. (2016). Complement and microglia mediate early synapse loss in Alzheimer mouse models. Science *352*, 712–716. 10.1126/science.aad8373.

36. Lui, H., Zhang, J., Makinson, S.R., Cahill, M.K., Kelley, K.W., Huang, H.-Y., Shang, Y., Oldham, M.C., Martens, L.H., Gao, F., et al. (2016). Progranulin Deficiency Promotes Circuit-Specific Synaptic Pruning by Microglia via Complement Activation. Cell *165*, 921–935. 10.1016/j.cell.2016.04.001.

37. Wohleb, E.S., Terwilliger, R., Duman, C.H., and Duman, R.S. (2018). Stress-Induced Neuronal Colony Stimulating Factor 1 Provokes Microglia-Mediated Neuronal Remodeling and Depressive-like Behavior. Biol. Psychiatry *83*, 38–49. 10.1016/j.biopsych.2017.05.026.

38. Zhang, M.-M., Guo, M.-X., Zhang, Q.-P., Chen, X.-Q., Li, N.-Z., Liu, Q., Cheng, J., Wang, S.-L., Xu, G.-H., Li, C.-F., et al. (2022). IL-1R/C3aR signaling regulates synaptic pruning in the prefrontal cortex of depression. Cell Biosci. *12*, 90. 10.1186/s13578-022-00832-4.

39. Wang, J., Chen, H.-S., Li, H.-H., Wang, H.-J., Zou, R.-S., Lu, X.-J., Wang, J., Nie, B.-B., Wu, J.-F., Li, S., et al. (2022). Microglia-dependent excessive synaptic pruning leads to cortical underconnectivity and behavioral abnormality following chronic social defeat stress in mice. Brain. Behav. Immun. 10.1016/j.bbi.2022.12.019.

40. Hammond, T.R., Dufort, C., Dissing-Olesen, L., Giera, S., Young, A., Wysoker, A., Walker, A.J., Gergits, F., Segel, M., Nemesh, J., et al. (2019). Single-Cell RNA Sequencing of Microglia throughout the Mouse Lifespan and in the Injured Brain Reveals Complex Cell-State Changes. Immunity *50*, 253-271.e6. 10.1016/j.immuni.2018.11.004.

41. Marsh, S.E., Kamath, T., Walker, A.J., Dissing-Olesen, L., Hammond, T.R., Young, A.M.H., Abdulraouf, A., Nadaf, N., Dufort, C., Murphy, S., et al. (2020). Single Cell Sequencing Reveals Glial Specific Responses to Tissue Processing & Enzymatic Dissociation in Mice and Humans 10.1101/2020.12.03.408542.

42. Safaiyan, S., Besson-Girard, S., Kaya, T., Cantuti-Castelvetri, L., Liu, L., Ji, H., Schifferer, M., Gouna, G., Usifo, F., Kannaiyan, N., et al. (2021). White matter aging drives microglial diversity. Neuron *109*, 1100-1117.e10. 10.1016/j.neuron.2021.01.027.

43. Stogsdill, J.A., Kim, K., Binan, L., Farhi, S.L., Levin, J.Z., and Arlotta, P. (2022). Pyramidal neuron subtype diversity governs microglia states in the neocortex. Nature, 1–7. 10.1038/s41586-022-05056-7.

44. Keren-Shaul, H., Spinrad, A., Weiner, A., Matcovitch-Natan, O., Dvir-Szternfeld, R., Ulland, T.K., David, E., Baruch, K., Lara-Astaiso, D., Toth, B., et al. (2017). A Unique Microglia Type Associated with Restricting Development of Alzheimer's Disease. Cell *169*, 1276-1290.e17. 10.1016/j.cell.2017.05.018.

45. Mathys, H., Davila-Velderrain, J., Peng, Z., Gao, F., Mohammadi, S., Young, J.Z., Menon, M., He, L., Abdurrob, F., Jiang, X., et al. (2019). Single-cell transcriptomic analysis of Alzheimer's disease. Nature *570*, 332–337. 10.1038/s41586-019-1195-2.

46. Olah, M., Menon, V., Habib, N., Taga, M.F., Ma, Y., Yung, C.J., Cimpean, M., Khairallah, A., Coronas-Samano, G., Sankowski, R., et al. (2020). Single cell RNA sequencing of human microglia uncovers a subset associated with Alzheimer's disease. Nat. Commun. *11*, 6129. 10.1038/s41467-020-19737-2.

47. Shoji, H., and Miyakawa, T. (2020). Differential effects of stress exposure via two types of restraint apparatuses on behavior and plasma corticosterone level in inbred male BALB/cAJcl mice. Neuropsychopharmacol. Rep. *40*, 73–84. 10.1002/npr2.12093.

48. Gong, S., Miao, Y.-L., Jiao, G.-Z., Sun, M.-J., Li, H., Lin, J., Luo, M.-J., and Tan, J.-H. (2015). Dynamics and Correlation of Serum Cortisol and Corticosterone under Different Physiological or Stressful Conditions in Mice. PLOS ONE *10*, e0117503. 10.1371/journal.pone.0117503.

49. Ding, J.X., Rudak, P.T., Inoue, W., and Haeryfar, S.M.M. (2021). Physical restraint mouse models to assess immune responses under stress with or without habituation. STAR Protoc. *2*, 100838. 10.1016/j.xpro.2021.100838.

50. Li, J., Xie, X., Li, Y., Liu, X., Liao, X., Su, Y.-A., and Si, T. (2017). Differential Behavioral and Neurobiological Effects of Chronic Corticosterone Treatment in Adolescent and Adult Rats. Front. Mol. Neurosci. *10*, 25. 10.3389/fnmol.2017.00025.

51. Marsh, S.E., Walker, A.J., Kamath, T., Dissing-Olesen, L., Hammond, T.R., de Soysa, T.Y., Young, A.M.H., Murphy, S., Abdulraouf, A., Nadaf, N., et al. (2022). Dissection of artifactual and confounding glial signatures by single-cell sequencing of mouse and human brain. Nat. Neurosci. *25*, 306–316. 10.1038/s41593-022-01022-8.

52. Li, Q., Cheng, Z., Zhou, L., Darmanis, S., Neff, N.F., Okamoto, J., Gulati, G., Bennett, M.L., Sun, L.O., Clarke, L.E., et al. (2019). Developmental Heterogeneity of Microglia and Brain Myeloid Cells Revealed by Deep Single-Cell RNA Sequencing. Neuron *101*, 207-223.e10. 10.1016/j.neuron.2018.12.006.

53. Corder, E.H., Saunders, A.M., Strittmatter, W.J., Schmechel, D.E., Gaskell, P.C., Small, G.W., Roses, A.D., Haines, J.L., and Pericak-Vance, M.A. (1993). Gene dose of apolipoprotein E type 4 allele and the risk of Alzheimer's disease in late onset families. Science *261*, 921–923. 10.1126/science.8346443.

54. Strittmatter, W.J., Saunders, A.M., Schmechel, D., Pericak-Vance, M., Enghild, J., Salvesen, G.S., and Roses, A.D. (1993). Apolipoprotein E: high-avidity binding to beta-amyloid and increased frequency of type 4 allele in late-onset familial Alzheimer disease. Proc. Natl. Acad. Sci. U. S. A. *90*, 1977–1981. 10.1073/pnas.90.5.1977.

55. Deming, Y., Filipello, F., Cignarella, F., Cantoni, C., Hsu, S., Mikesell, R., Li, Z., Del-Aguila, J.L., Dube, U., Farias, F.G., et al. (2019). The MS4A gene cluster is a key modulator

of soluble TREM2 and Alzheimer's disease risk. Sci. Transl. Med. *11*, eaau2291. 10.1126/scitranslmed.aau2291.

56. Festa, B.P., Siddiqi, F.H., Jimenez-Sanchez, M., Won, H., Rob, M., Djajadikerta, A., Stamatakou, E., and Rubinsztein, D.C. (2023). Microglial-to-neuronal CCR5 signaling regulates autophagy in neurodegeneration. Neuron. 10.1016/j.neuron.2023.04.006.

57. Escoubas, C.C., Dorman, L.C., Nguyen, P.T., Lagares-Linares, C., Nakajo, H., Anderson, S.R., Cuevas, B., Vainchtein, I.D., Silva, N.J., Xiao, Y., et al. (2023). Type I interferon responsive microglia shape cortical development and behavior. BioRxiv Prepr. Serv. Biol., 2021.04.29.441889. 10.1101/2021.04.29.441889.

58. Arnsten, A.F.T. (2009). Stress signalling pathways that impair prefrontal cortex structure and function. Nat. Rev. Neurosci. *10*, 410–422. 10.1038/nrn2648.

59. Chen, C.-C., Lu, J., Yang, R., Ding, J.B., and Zuo, Y. (2018). Selective activation of parvalbumin interneurons prevents stress-induced synapse loss and perceptual defects. Mol. Psychiatry *23*, 1614–1625. 10.1038/mp.2017.159.

60. Liston, C., and Gan, W.-B. (2011). Glucocorticoids are critical regulators of dendritic spine development and plasticity in vivo. Proc. Natl. Acad. Sci. *108*, 16074–16079. 10.1073/pnas.1110444108.

61. Cong, Q., Soteros, B.M., Huo, A., Li, Y., Tenner, A.J., and Sia, G.M. (2022). C1q and SRPX2 regulate microglia mediated synapse elimination during early development in the visual thalamus but not the visual cortex. Glia *70*, 451–465. 10.1002/glia.24114.

62. Bolkan, S.S., Stujenske, J.M., Parnaudeau, S., Spellman, T.J., Rauffenbart, C., Abbas, A.I., Harris, A.Z., Gordon, J.A., and Kellendonk, C. (2017). Thalamic projections sustain prefrontal activity during working memory maintenance. Nat. Neurosci. *20*, 987–996. 10.1038/nn.4568.

63. Schmitt, L.I., Wimmer, R.D., Nakajima, M., Happ, M., Mofakham, S., and Halassa, M.M. (2017). Thalamic amplification of cortical connectivity sustains attentional control. Nature *545*, 219–223. 10.1038/nature22073.

64. Parnaudeau, S., O'Neill, P.-K., Bolkan, S.S., Ward, R.D., Abbas, A.I., Roth, B.L., Balsam, P.D., Gordon, J.A., and Kellendonk, C. (2013). Inhibition of mediodorsal thalamus disrupts thalamofrontal connectivity and cognition. Neuron *77*, 1151–1162. 10.1016/j.neuron.2013.01.038.

65. Jett, J.D., Bulin, S.E., Hatherall, L.C., McCartney, C.M., and Morilak, D.A. (2017). Deficits in cognitive flexibility induced by chronic unpredictable stress are associated with impaired glutamate neurotransmission in the rat medial prefrontal cortex. Neuroscience *346*, 284–297. 10.1016/j.neuroscience.2017.01.017.

66. Stevens, B., Allen, N.J., Vazquez, L.E., Howell, G.R., Christopherson, K.S., Nouri, N., Micheva, K.D., Mehalow, A.K., Huberman, A.D., Stafford, B., et al. (2007). The classical complement cascade mediates CNS synapse elimination. Cell *131*, 1164–1178.

67. Crider, A., Feng, T., Pandya, C.D., Davis, T., Nair, A., Ahmed, A.O., Baban, B., Turecki, G., and Pillai, A. (2018). Complement component 3a receptor deficiency attenuates chronic stress-induced monocyte infiltration and depressive-like behavior. Brain. Behav. Immun. *70*, 246–256. 10.1016/j.bbi.2018.03.004.

68. Haykin, H., and Rolls, A. (2021). The neuroimmune response during stress: A physiological perspective. Immunity *54*, 1933–1947. 10.1016/j.immuni.2021.08.023.

69. Wang, S., Sudan, R., Peng, V., Zhou, Y., Du, S., Yuede, C.M., Lei, T., Hou, J., Cai, Z., Cella, M., et al. (2022). TREM2 drives microglia response to amyloid-β via SYK-dependent and -independent pathways. Cell *185*, 4153-4169.e19. 10.1016/j.cell.2022.09.033.

70. Srinivasan, K., Friedman, B.A., Etxeberria, A., Huntley, M.A., van der Brug, M.P., Foreman, O., Paw, J.S., Modrusan, Z., Beach, T.G., Serrano, G.E., et al. (2020). Alzheimer's Patient Microglia Exhibit Enhanced Aging and Unique Transcriptional Activation. Cell Rep. *31*, 107843. 10.1016/j.celrep.2020.107843.

71. Krasemann, S., Madore, C., Cialic, R., Baufeld, C., Calcagno, N., El Fatimy, R., Beckers, L., O'Loughlin, E., Xu, Y., Fanek, Z., et al. (2017). The TREM2-APOE Pathway Drives the Transcriptional Phenotype of Dysfunctional Microglia in Neurodegenerative Diseases. Immunity *47*, 566-581.e9. 10.1016/j.immuni.2017.08.008.

72. Tansley, S., Uttam, S., Ureña Guzmán, A., Yaqubi, M., Pacis, A., Parisien, M., Deamond, H., Wong, C., Rabau, O., Brown, N., et al. (2022). Single-cell RNA sequencing reveals time- and sex-specific responses of mouse spinal cord microglia to peripheral nerve injury and links ApoE to chronic pain. Nat. Commun. *13*, 843. 10.1038/s41467-022-28473-8.

73. Frigerio, C.S., Wolfs, L., Fattorelli, N., Thrupp, N., Voytyuk, I., Schmidt, I., Mancuso, R., Chen, W.-T., Woodbury, M.E., Srivastava, G., et al. (2019). The Major Risk Factors for Alzheimer's Disease: Age, Sex, and Genes Modulate the Microglia Response to Aβ Plaques. Cell Rep. *27*, 1293-1306.e6. 10.1016/j.celrep.2019.03.099.

74. Absinta, M., Maric, D., Gharagozloo, M., Garton, T., Smith, M.D., Jin, J., Fitzgerald, K.C., Song, A., Liu, P., Lin, J.-P., et al. (2021). A lymphocyte-microglia-astrocyte axis in chronic active multiple sclerosis. Nature. 10.1038/s41586-021-03892-7.

75. Selye, H. (1936). A Syndrome produced by Diverse Nocuous Agents. Nature *138*, 32–32. 10.1038/138032a0.

76. Selye, H. (1950). Stress and the general adaptation syndrome. Br. Med. J. *1*, 1383–1392. 10.1136/bmj.1.4667.1383.

77. Ayata, P., Badimon, A., Strasburger, H.J., Duff, M.K., Montgomery, S.E., Loh, Y.-H.E., Ebert, A., Pimenova, A.A., Ramirez, B.R., Chan, A.T., et al. (2018). Epigenetic regulation of

brain region-specific microglia clearance activity. Nat. Neurosci. *21*, 1049–1060. 10.1038/s41593-018-0192-3.

78. McQuade, A., Kang, Y.J., Hasselmann, J., Jairaman, A., Sotelo, A., Coburn, M., Shabestari, S.K., Chadarevian, J.P., Fote, G., Tu, C.H., et al. (2020). Gene expression and functional deficits underlie TREM2-knockout microglia responses in human models of Alzheimer's disease. Nat. Commun. *11*, 5370. 10.1038/s41467-020-19227-5.

79. Mazaheri, F., Snaidero, N., Kleinberger, G., Madore, C., Daria, A., Werner, G., Krasemann, S., Capell, A., Trümbach, D., Wurst, W., et al. (2017). TREM2 deficiency impairs chemotaxis and microglial responses to neuronal injury. EMBO Rep. *18*, 1186–1198. 10.15252/embr.201743922.

80. Shi, Q., Chowdhury, S., Ma, R., Le, K.X., Hong, S., Caldarone, B.J., Stevens, B., and Lemere, C.A. (2017). Complement C3 deficiency protects against neurodegeneration in aged plaque-rich APP/PS1 mice. Sci. Transl. Med. *9*, eaaf6295. 10.1126/scitranslmed.aaf6295.

81. Dejanovic, B., Huntley, M.A., De Mazière, A., Meilandt, W.J., Wu, T., Srinivasan, K., Jiang, Z., Gandham, V., Friedman, B.A., Ngu, H., et al. (2018). Changes in the Synaptic Proteome in Tauopathy and Rescue of Tau-Induced Synapse Loss by C1q Antibodies. Neuron. 10.1016/j.neuron.2018.10.014.

82. Werneburg, S., Jung, J., Kunjamma, R.B., Ha, S.-K., Luciano, N.J., Willis, C.M., Gao, G., Biscola, N.P., Havton, L.A., Crocker, S.J., et al. (2020). Targeted Complement Inhibition at Synapses Prevents Microglial Synaptic Engulfment and Synapse Loss in Demyelinating Disease. Immunity *52*, 167-182.e7. 10.1016/j.immuni.2019.12.004.

83. Hammond, J.W., Bellizzi, M.J., Ware, C., Qiu, W.Q., Saminathan, P., Li, H., Luo, S., Ma, S.A., Li, Y., and Gelbard, H.A. (2020). Complement-dependent synapse loss and microgliosis in a mouse model of multiple sclerosis. Brain. Behav. Immun. 10.1016/j.bbi.2020.03.004.

84. Qiao, H., Li, M.-X., Xu, C., Chen, H.-B., An, S.-C., and Ma, X.-M. (2016). Dendritic Spines in Depression: What We Learned from Animal Models. Neural Plast. *2016*. 10.1155/2016/8056370.

85. Duman, C.H., and Duman, R.S. (2015). Spine synapse remodeling in the pathophysiology and treatment of depression. Neurosci. Lett. *601*, 20–29. 10.1016/j.neulet.2015.01.022.

86. Arnsten, A.F.T., Woo, E., Yang, S., Wang, M., and Datta, D. (2022). Unusual Molecular Regulation of Dorsolateral Prefrontal Cortex Layer III Synapses Increases Vulnerability to Genetic and Environmental Insults in Schizophrenia. Biol. Psychiatry *92*, 480–490. 10.1016/j.biopsych.2022.02.003.

87. Berdenis van Berlekom, A., Muflihah, C.H., Snijders, G.J.L.J., MacGillavry, H.D., Middeldorp, J., Hol, E.M., Kahn, R.S., and de Witte, L.D. (2020). Synapse Pathology in Schizophrenia: A Meta-analysis of Postsynaptic Elements in Postmortem Brain Studies. Schizophr. Bull. *46*, 374–386. 10.1093/schbul/sbz060.

88. Glantz, L.A., and Lewis, D.A. (2000). Decreased dendritic spine density on prefrontal cortical pyramidal neurons in schizophrenia. Arch. Gen. Psychiatry *57*, 65–73.

89. Kolluri, N., Sun, Z., Sampson, A.R., and Lewis, D.A. (2005). Lamina-specific reductions in dendritic spine density in the prefrontal cortex of subjects with schizophrenia. Am. J. Psychiatry *162*, 1200–1202. 10.1176/appi.ajp.162.6.1200.

90. Holtzman, C.W., Trotman, H.D., Goulding, S.M., Ryan, A.T., Macdonald, A.N., Shapiro, D.I., Brasfield, J.L., and Walker, E.F. (2013). Stress and neurodevelopmental processes in the emergence of psychosis. Neuroscience *249*, 172–191. 10.1016/j.neuroscience.2012.12.017.

91. Lei, Y., Wang, J., Wang, D., Li, C., Liu, B., Fang, X., You, J., Guo, M., and Lu, X.-Y. (2020). SIRT1 in forebrain excitatory neurons produces sexually dimorphic effects on depression-related behaviors and modulates neuronal excitability and synaptic transmission in the medial prefrontal cortex. Mol. Psychiatry *25*, 1094–1111. 10.1038/s41380-019-0352-1.

92. Zhu, X., Tang, H.-D., Dong, W.-Y., Kang, F., Liu, A., Mao, Y., Xie, W., Zhang, X., Cao, P., Zhou, W., et al. (2021). Distinct thalamocortical circuits underlie allodynia induced by tissue injury and by depression-like states. Nat. Neurosci. *24*, 542–553. 10.1038/s41593-021-00811-x.

93. Stuart, T., Butler, A., Hoffman, P., Hafemeister, C., Papalexi, E., Mauck, W.M., Hao, Y., Stoeckius, M., Smibert, P., and Satija, R. (2019). Comprehensive Integration of Single-Cell Data. Cell *177*, 1888-1902.e21. 10.1016/j.cell.2019.05.031.

94. Choudhary, S., and Satija, R. (2022). Comparison and evaluation of statistical error models for scRNA-seq. Genome Biol. *23*, 27. 10.1186/s13059-021-02584-9.

95. McGinnis, C.S., Murrow, L.M., and Gartner, Z.J. (2019). DoubletFinder: Doublet Detection in Single-Cell RNA Sequencing Data Using Artificial Nearest Neighbors. Cell Syst. *8*, 329-337.e4. 10.1016/j.cels.2019.03.003.

96. Blighe, K., Rana, S., and Lewis, M. (2018). EnhancedVolcano: publication-ready volcano plots with enhanced colouring and labeling.

97. Trapnell, C., Cacchiarelli, D., Grimsby, J., Pokharel, P., Li, S., Morse, M., Lennon, N.J., Livak, K.J., Mikkelsen, T.S., and Rinn, J.L. (2014). The dynamics and regulators of cell fate decisions are revealed by pseudotemporal ordering of single cells. Nat. Biotechnol. *32*, 381–386. 10.1038/nbt.2859.

98. Yu, G., Wang, L.-G., Han, Y., and He, Q.-Y. (2012). clusterProfiler: an R Package for Comparing Biological Themes Among Gene Clusters. OMICS J. Integr. Biol. *16*, 284–287. 10.1089/omi.2011.0118.

99. Cruz-Sanchez, A., Dematagoda, S., Ahmed, R., Mohanathaas, S., Odenwald, N., and Arruda-Carvalho, M. (2020). Developmental onset distinguishes three types of spontaneous recognition memory in mice. Sci. Rep. *10*, 10612. 10.1038/s41598-020-67619-w.

Figure 1

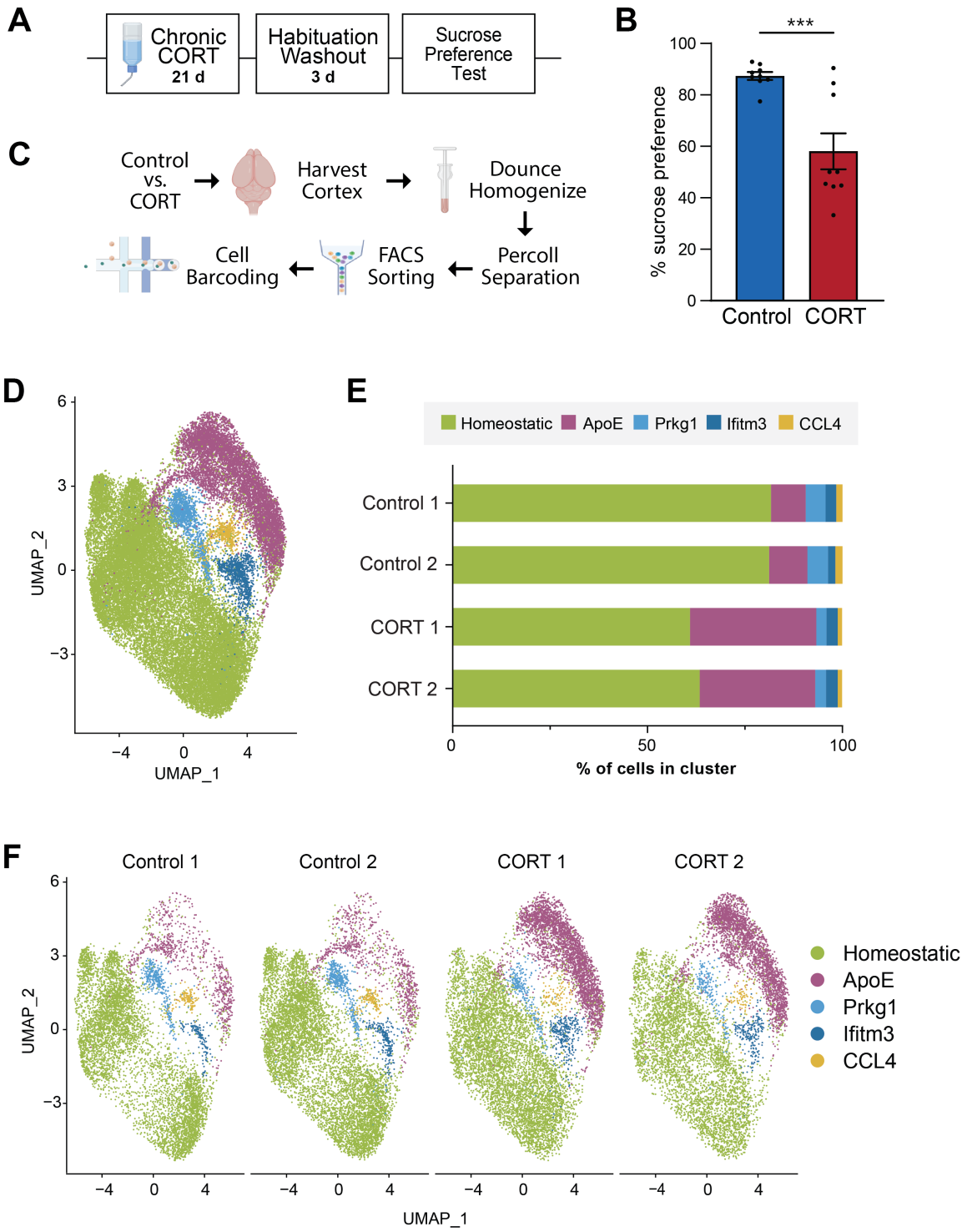
A
Chronic CORT 21 d
Habituation Washout 3 d
Sucrose Preference Test
B
***
% sucrose preference
100
80
60
40
20
0
Control
CORT
C
Control vs. CORT
Harvest Cortex
Dounce Homogenize
Percoll Separation
FACS Sorting
Cell Barcoding
D
UMAP_2
UMAP_1
6
3
0
−3
−4
0
4
E
Homeostatic
ApoE
Prkg1
Ifitm3
CCL4
Control 1
Control 2
CORT 1
CORT 2
0
50
100
% of cells in cluster
F
Control 1
Control 2
CORT 1
CORT 2
UMAP_2
UMAP_1
Homeostatic
ApoE
Prkg1
Ifitm3
CCL4

Figure 2

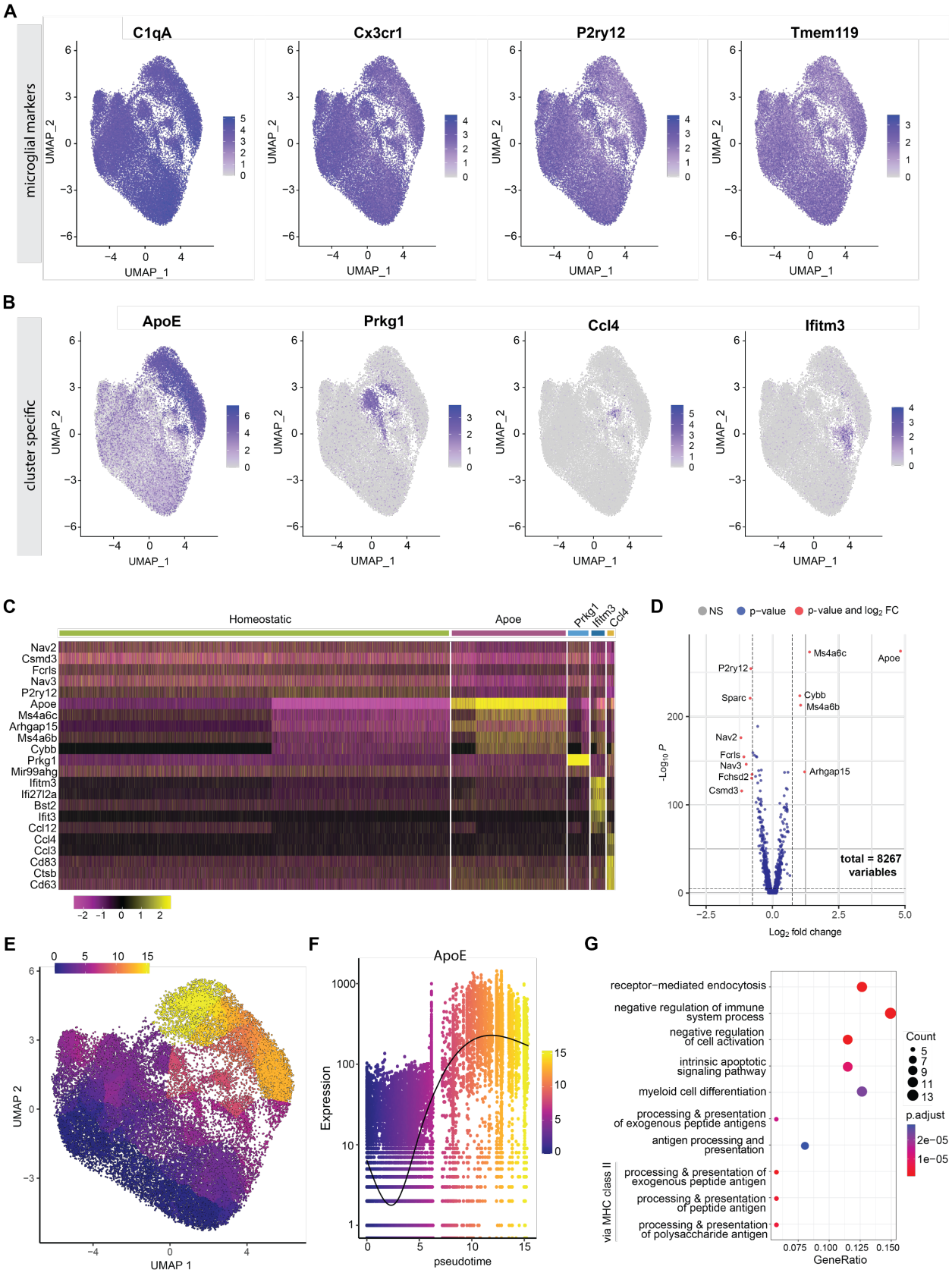
A
microglial markers
C1qA
Cx3cr1
P2ry12
Tmem119
UMAP_1
UMAP_2
B
cluster specific
ApoE
Prkg1
Ccl4
Ifitm3
C
Homeostatic
Apoe
Prkg1
Ifitm3
Ccl4
Nav2
Csmd3
Fcrls
Nav3
P2ry12
Apoe
Ms4a6c
Arhgap15
Ms4a6b
Cybb
Prkg1
Mir99ahg
Ifitm3
Ifi27l2a
Bst2
Ifit3
Ccl12
Ccl4
Ccl3
Cd83
Ctsb
Cd63
D
NS
p-value
p-value and log2 FC
Ms4a6c
Apoe
P2ry12
Sparc
Cybb
Ms4a6b
Nav2
Fcrls
Nav3
Fchsd2
Csmd3
Arhgap15
total = 8267 variables
-Log10 P
Log2 fold change
E
UMAP 1
UMAP 2
F
ApoE
Expression
pseudotime
G
receptor−mediated endocytosis
negative regulation of immune system process
negative regulation of cell activation
intrinsic apoptotic signaling pathway
myeloid cell differentiation
processing & presentation of exogenous peptide antigens
antigen processing and presentation
processing & presentation of exogenous peptide antigen via MHC class II
processing & presentation of peptide antigen
processing & presentation of polysaccharide antigen
GeneRatio
Count
p.adjust

Figure 3

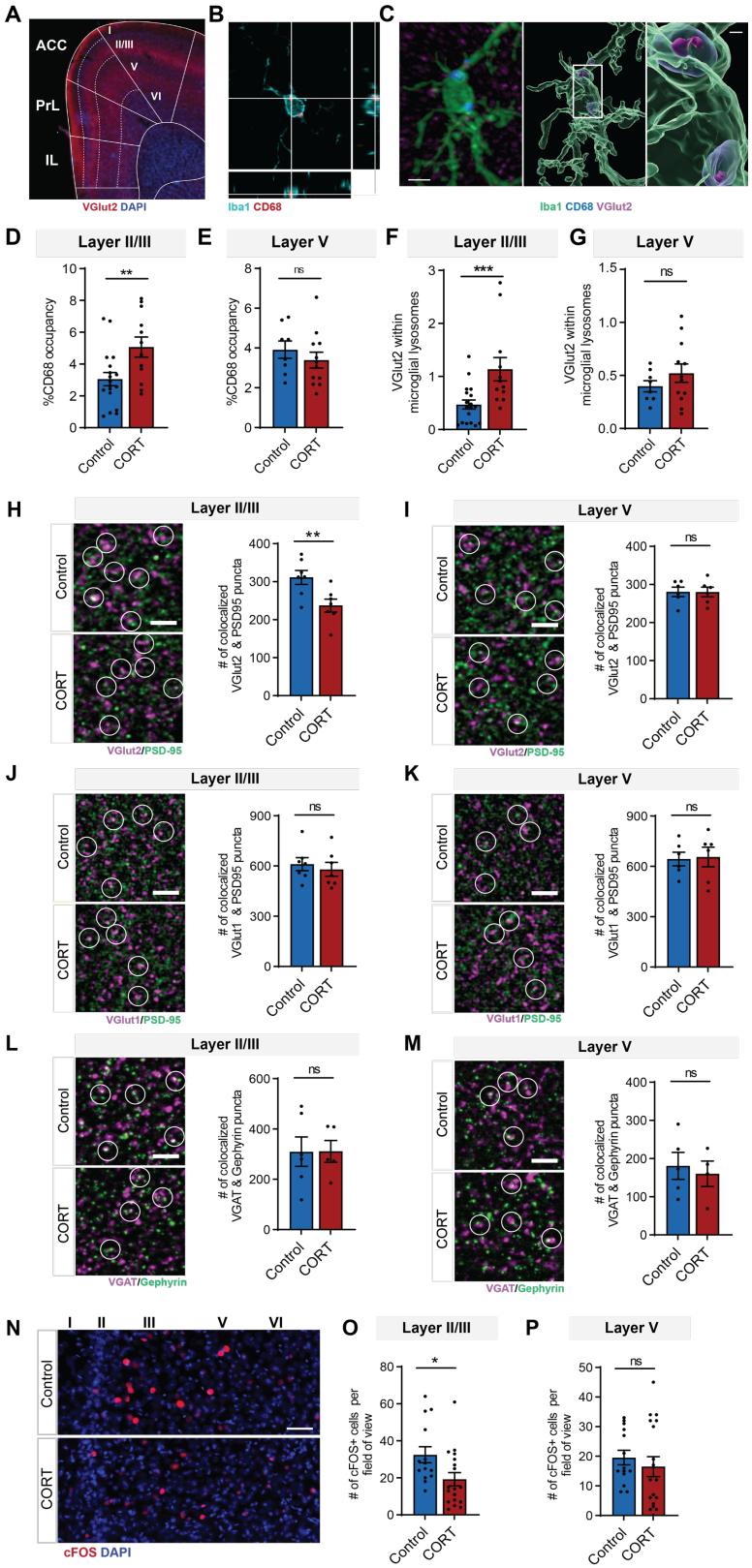
A
ACC
PrL
IL
I
II/III
V
VI
VGlut2 DAPI
B
Iba1 CD68
C
Iba1 CD68 VGlut2
D
Layer II/III
%CD68 occupancy
**
Control
CORT
E
Layer V
%CD68 occupancy
ns
F
Layer II/III
VGlut2 within microglial lysosomes
***
G
Layer V
VGlut2 within microglial lysosomes
ns
H
Layer II/III
Control
CORT
VGlut2/PSD-95
# of colocalized VGlut2 & PSD95 puncta
**
I
Layer V
# of colocalized VGlut2 & PSD95 puncta
ns
J
Layer II/III
VGlut1/PSD-95
# of colocalized VGlut1 & PSD95 puncta
ns
K
Layer V
# of colocalized VGlut1 & PSD95 puncta
ns
L
Layer II/III
VGAT/Gephyrin
# of colocalized VGAT & Gephyrin puncta
ns
M
Layer V
# of colocalized VGAT & Gephyrin puncta
ns
N
I
II
III
V
VI
cFOS DAPI
O
Layer II/III
# of cFOS+ cells per field of view
*
P
Layer V
# of cFOS+ cells per field of view
ns

Figure 4

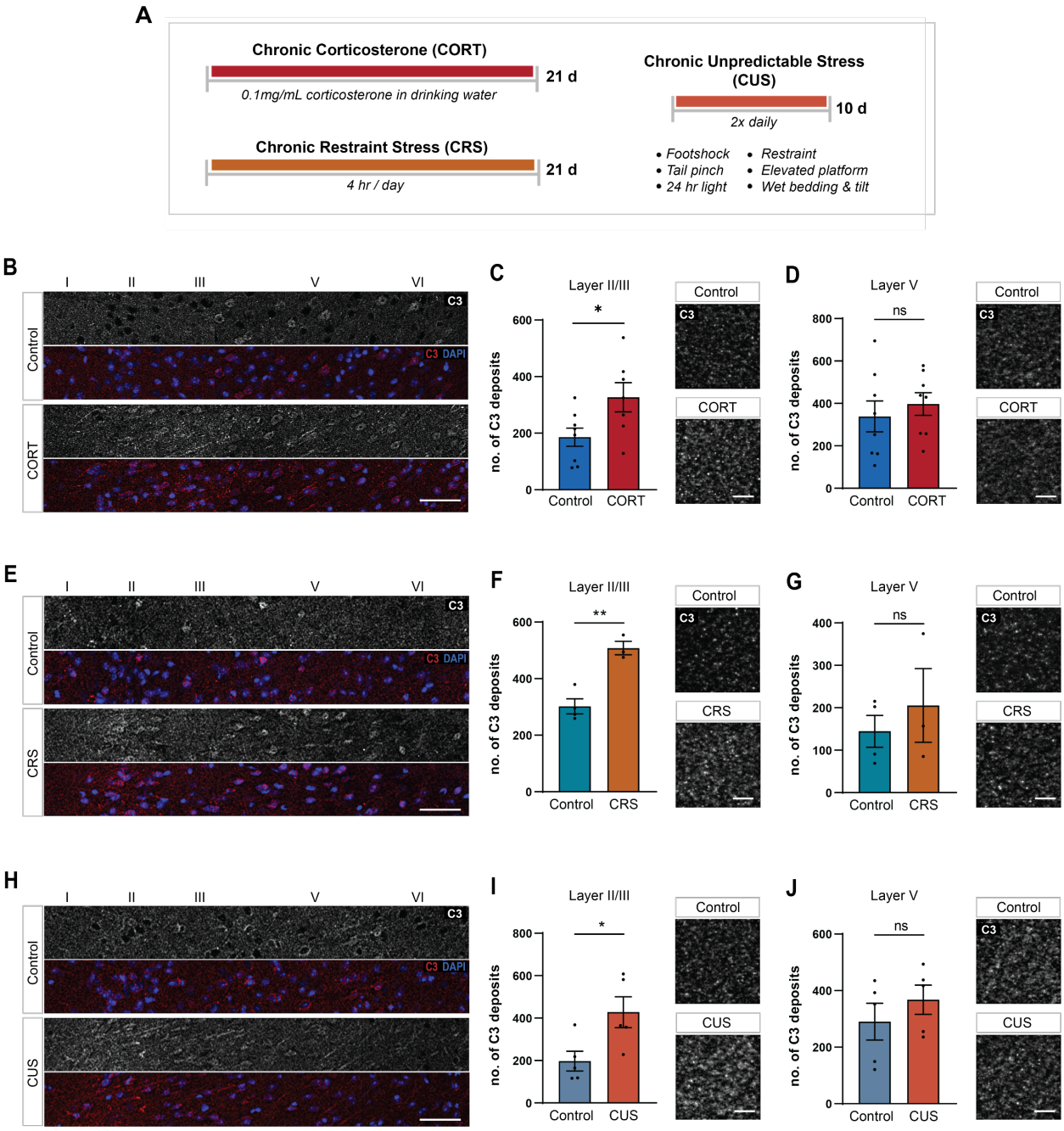
A
Chronic Corticosterone (CORT)
21 d
0.1mg/mL corticosterone in drinking water
Chronic Restraint Stress (CRS)
21 d
4 hr / day
Chronic Unpredictable Stress (CUS)
10 d
2x daily
• Footshock
• Tail pinch
• 24 hr light
• Restraint
• Elevated platform
• Wet bedding & tilt
B
I
II
III
V
VI
C3
C3 DAPI
Control
CORT
C
Layer II/III
no. of C3 deposits
Control
CORT
D
Layer V
ns
E
CRS
F
G
H
CUS
I
J

Figure 5

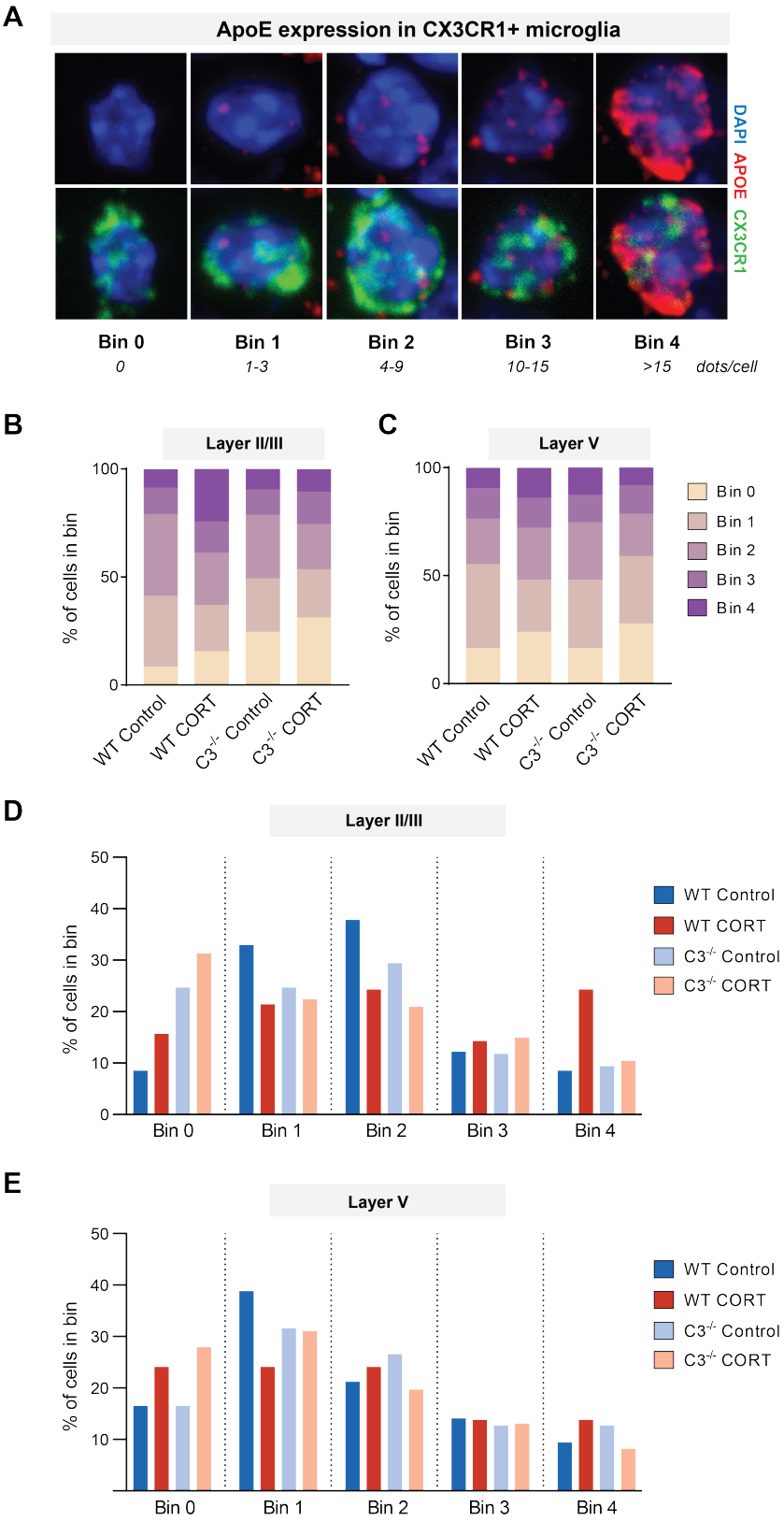
A
ApoE expression in CX3CR1+ microglia
DAPI
APOE
CX3CR1
Bin 0
0
Bin 1
1-3
Bin 2
4-9
Bin 3
10-15
Bin 4
>15
dots/cell
B
Layer II/III
% of cells in bin
100
50
0
WT Control
WT CORT
C3-/- Control
C3-/- CORT
C
Layer V
Bin 0
Bin 1
Bin 2
Bin 3
Bin 4
D
Layer II/III
50
40
30
20
10
WT Control
WT CORT
C3-/- Control
C3-/- CORT
E
Layer V

Figure 6

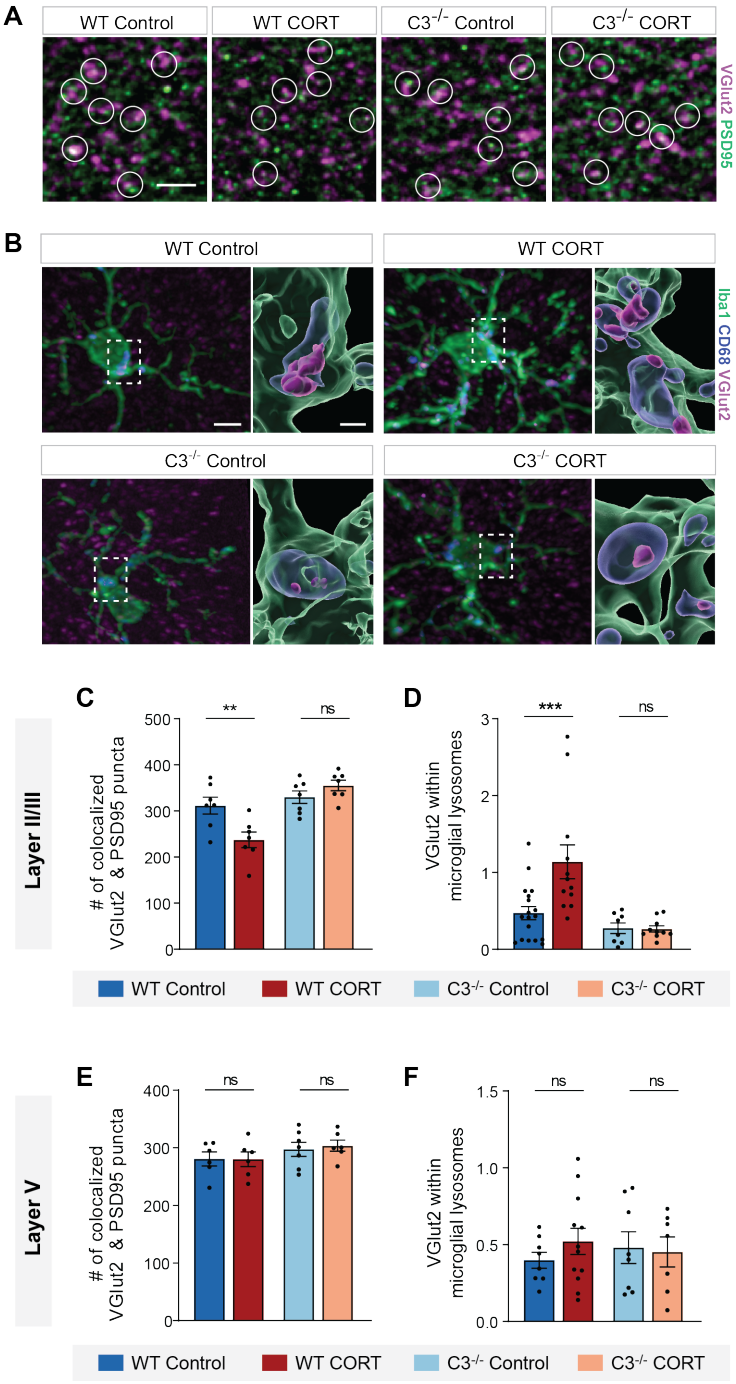
A
WT Control
WT CORT
C3-/- Control
C3-/- CORT
VGlut2 PSD95
B
WT Control
WT CORT
C3-/- Control
C3-/- CORT
Iba1 CD68 VGlut2
Layer II/III
C
# of colocalized VGlut2 & PSD95 puncta
**
ns
D
VGlut2 within microglial lysosomes
***
ns
WT Control
WT CORT
C3-/- Control
C3-/- CORT
Layer V
E
# of colocalized VGlut2 & PSD95 puncta
ns
ns
F
VGlut2 within microglial lysosomes
ns
ns
WT Control
WT CORT
C3-/- Control
C3-/- CORT

Figure 7

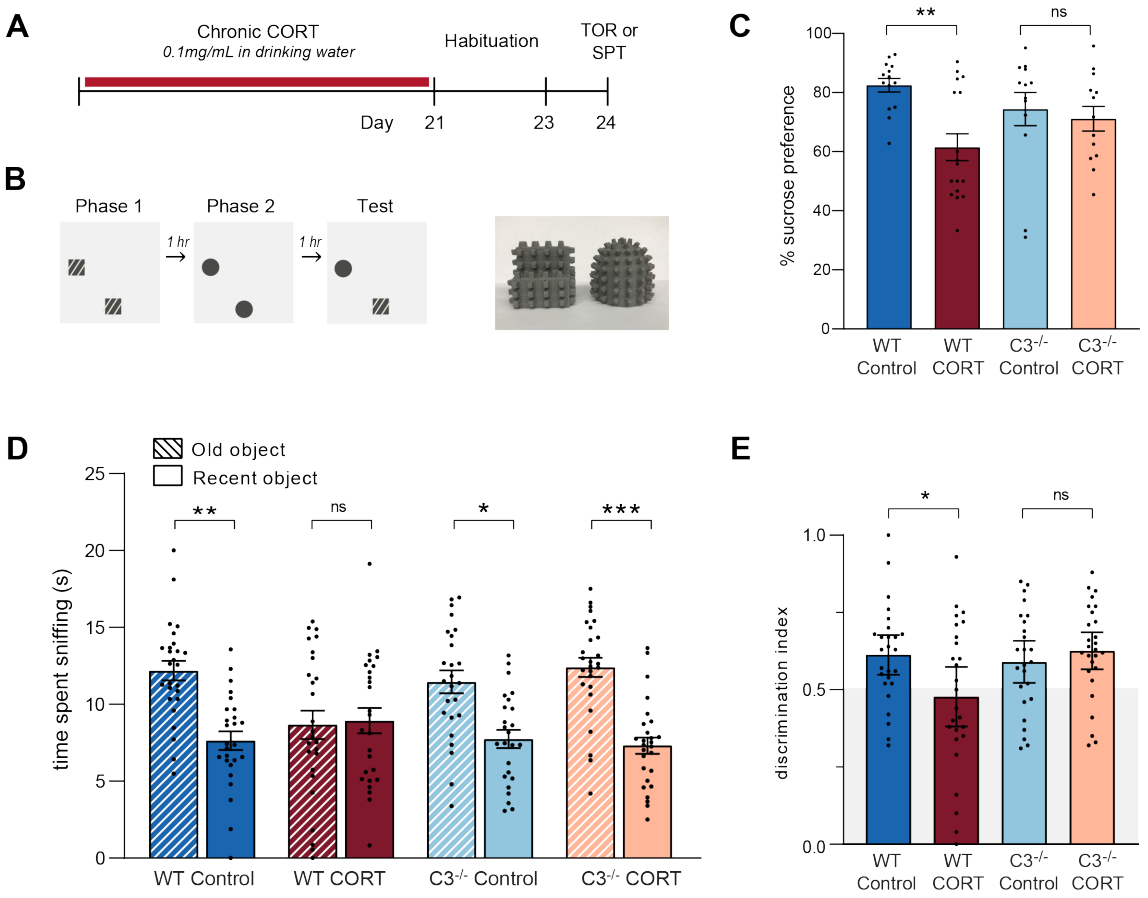
A
Chronic CORT
0.1mg/mL in drinking water
Habituation
TOR or SPT
Day
21
23
24
B
Phase 1
Phase 2
Test
1 hr
1 hr
C
% sucrose preference
**
ns
WT Control
WT CORT
C3-/- Control
C3-/- CORT
D
Old object
Recent object
time spent sniffing (s)
**
ns
*
***
WT Control
WT CORT
C3-/- Control
C3-/- CORT
E
discrimination index
*
ns
WT Control
WT CORT
C3-/- Control
C3-/- CORT
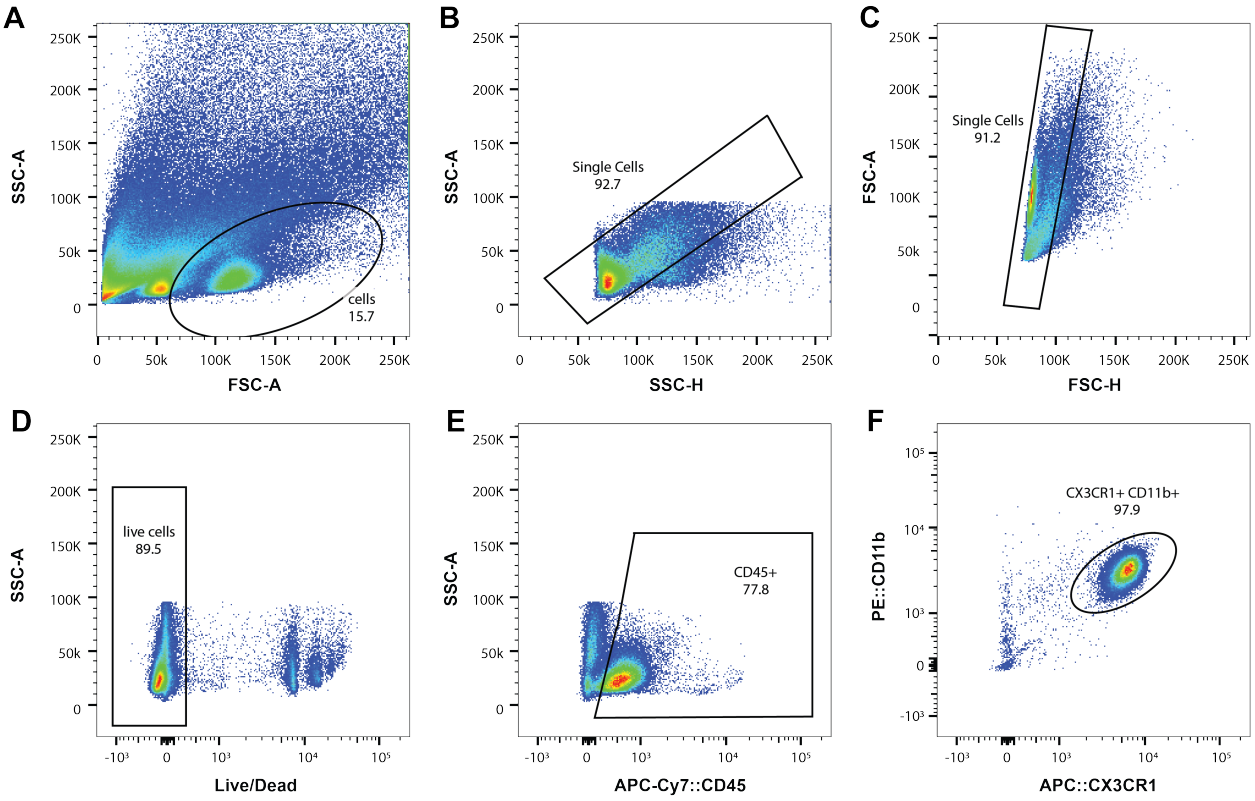
Supplementary Figure 1